SANTA CATARINA STATE UNIVERSITY - UDESC
COLLEGE OF TECHNOLOGICAL SCIENCE - CCT
MECHANICAL ENGINEERING GRADUATE PROGRAM - PPGEM

ALINI EMMANUELE GRACINSKI

A STUDY ON THE EFFECT OF POROSITY LEVEL AND DISTRIBUTION ON THE MODAL RESPONSE OF CASTED PARTS

JOINVILLE - SC
2021

ALINI EMMANUELE GRACINSKI

A STUDY ON THE EFFECT OF POROSITY LEVEL AND DISTRIBUTION ON THE MODAL RESPONSE OF CASTED PARTS

Master thesis submitted to the Mechanical Engineering Department at the College of Technological Science of Santa Catarina State University in fulfillment of the partial requirement for the Master's degree in Mechanical Engineering.

Adviser: Prof. Dr. Eduardo Lenz Cardoso

JOINVILLE - SC
2021

Gracinski, Alini
A study on the effect of porosity level and distribution on the modal response of casted parts / Alini Gracinski. -- 2021.
81 p.

Orientador: Eduardo Lenz Cardoso
Dissertação (mestrado) -- Universidade do Estado de Santa Catarina, Centro de Ciências Tecnológicas, Programa de Pós-Graduação em Engenharia Mecânica, Joinville, 2021.

1. Porosity. 2. Monte Carlo Simulation. 3. Damage Detection. 4. Natural Frequency. 5. Microporosity. I. Cardoso, Eduardo Lenz. II. Universidade do Estado de Santa Catarina, Centro de Ciências Tecnológicas, Programa de Pós-Graduação em Engenharia Mecânica. III. Título.

ALINI EMMANUELE GRACINSKI

A STUDY ON THE EFFECT OF POROSITY LEVEL AND DISTRIBUTION ON THE MODAL RESPONSE OF CASTED PARTS

Dissertação apresentada ao Programa de Pós-Graduação em Engenharia Mecânica do Centro de Ciências Tecnológicas da Universidade do Estado de Santa Catarina, como parte dos requisitos necessários para obtenção do título de Mestre em Engenharia Mecânica, área de concentração: Modelagem e Simulação Numérica.

BANCA EXAMINADORA

Orientador:

____

Prof. Dr. Eduardo Lenz Cardoso
Universidade do Estado de Santa Catarina
Departamento de Engenharia Mecânica

Membros:

____

Prof. Dr. Ricardo de Medeiros
Universidade do Estado de Santa Catarina
Departamento de Engenharia Mecânica

____

Prof. Dr. Olavo Mecias da Silva Junior
Universidade do Estado de Santa Catarina
Departamento de Engenharia Mecânica

Joinville, 30 de junho de 2021.

ACKNOWLEDGMENTS

The author would like to express the following acknowledgements.

To Prof. Dr. Eduardo Lenz Cardoso, for having the patience of a Saint and always being available to share and help me with his knowledge. Thank you for accepting to be my advisor for the second time.

To Diego Schmiit Montero, for the love, incentive, moral support and help at every step of the way. My life would not be the same without you.

To my parents, Noemi and Laudi, for the care and education given through all my life.

To the Professors, Professionals and colleagues of the Mechanical Engineering Graduate Program that contributed for my formation.

To the Santa Catarina State University for the high quality education provided.

This study was financed in part by the Coordenação de Aperfeiçoamento de Pessoal de Nível Superior - Brasil (CAPES) - Finance Code 001.

The authors acknowledge funding of this research project by Brazilian agency FAPESC (Fundação de Amparo à Pesquisa e Inovação do Estado de Santa Catarina, grants 2019TR779).

ABSTRACT

EMMANUELE GRACINSKI, ALINI, A STUDY ON THE EFFECT OF POROSITY LEVEL AND DISTRIBUTION ON THE MODAL RESPONSE OF CASTED PARTS . 2021. Master Thesis (Master in Mechanical Engineering - Area: Numerical Modeling and Simulation) – SANTA CATARINA STATE UNIVERSITY. MECHANICAL ENGINEERING GRADUATE PROGRAM Joinville 2021.

Microporosity is one the most recurrent problems in casting processes, which impacts the quality of the resulting parts, negatively affecting mechanical properties such as strength and fatigue life. The goal of this work is to contribute to the damage detection research field, by acquiring a better understanding of the effect of porosity in the natural frequency of structures. A criterion for the acceptable amount of porosity and a numerical model based on random porosity spacial distributions and levels is proposed. The Monte Carlo Simulation method is applied to investigate the effect of different levels of porosities and to infer the statistical nature of the frequency response. The influence of the different porosity levels and spatial distributions on natural frequency is acquired and discussed for specific structures. In this work two different test cases are investigated: isotropic beams and an L-shaped structure subject to different boundary conditions. The resulting natural frequencies are approximated by statistical distributions, and correlations between the boundary conditions and the levels and distribution of porosity are determined. Patterns for porosity identification regarding to levels and spatial distributions are obtained by using the first fourth natural frequencies from bending modes.

Key-words: Porosity, Microporosity, Monte Carlo Simulation, Damage Detection, Natural frequency

RESUMO

EMMANUELE GRACINSKI, ALINI, A STUDY ON THE EFFECT OF POROSITY LEVEL AND DISTRIBUTION ON THE MODAL RESPONSE OF CASTED PARTS. 2021. Dissertação (Mestrado em Engenharia Mecânica - Área: Modelagem e Simulação Numérica) – Universidade do Estado de Santa Catarina. Programa de Pós-Graduação em Engenharia Mecânica Joinville 2021.

Microporosidade é um problema recorrente no processo de fundição que impacta a qualidade final dos componentes, afetando negativamente as propriedades mecânicas, como resistência e vida em fadiga. O objetivo deste trabalho é contribuir na área de detecção de dano, adquirindo melhor compreensão sobre o efeito da porosidade na frequência natural de estruturas. É proposto um critério para quantidade aceitável de porosidade e um modelo numérico baseado em distribuições espaciais aleatórias e níveis de porosidade. O método de Simulação de Monte Carlo é aplicado para investigar o efeito de diferentes níveis de porosidade e entender sobre a natureza estatistica da resposta em frequência. A influência de diferentes níveis de porosidade e distribuições espaciais na frequência natural é obtida e discutida para estruturas específicas. Neste trabalho dois casos são investigados: Vigas isotrópicas e uma estrutura em formato L, submetidos a diferentes condições de contorno. As frequências naturais resultantes são aproximadas por distribuições estatísticas e as correlações entre as condições de contorno e os níveis e distribuições de porosidade são determinadas. Padrões para identificação de quantidade e distribuições espaciais de porosidades são obtidos utilizando as quatro primeiras frequências naturais de modos de flexão.

Palavras-chave: Porosidade, Microporosidade, Simulação de Monte Carlo, Detecção de dano, Frequência natural

List of Figures

List of Tables

Table of Contents

Chapter 1

Introduction

Porosity is one of the types of discontinuity that can be present in materials, usually due to issues in the manufacturing process. ASTM E505-15 (2000) defines the visual appearance of porosity in metallography as "Round or elongated, smooth-edged dark spots occurring individually distributed or in clusters". Porosities are present in all types of materials, however it is frequently associated with casted components, since the foundry process is hard to control.

For non-severe applications, such as components with reduced or no loading, defects such as porosities can be allowed when still satisfies the performance requirements, but for certain applications, the porosity level is a characteristic critical to quality.

Casting imperfections are specially troublesome as they are difficult to prevent. Foundry processes are sensitive to mold and part design, fill rates, temperature gradients, and other variables that can be hard to control. The most common types of defects in casting are cold fills, alumina skins, and entrapped air bubbles (AVALLE et al., 2002).

Although the casting process is complicated to control, casting components usually have good cost-benefit, allowing complicated geometry manufacturing, along with good mechanical properties. These components are present in industries such as automotive, electrical rotating machines, and wind turbines, where the level of defects must be minimal to ensure safe operation.

As porosity undermines material performance characteristics, such as reduction of fatigue life and material elongation (LEE et al., 2001), it is one of the most studied casting defects. There are three main research fields in casting porosity formation: numerical modelling of the formation process, understanding the effects caused by porosity presence, and porosity detection in manufactured components.

The porosity formation modelling process goes a long way back, since Piwonka e Flemings (1966) started to model shrinkage porosity formation during the solidification process, to recent studies as Khalajzadeh et al. (2018), where significant discoveries are being made in predicting microporosity and others castings defects using numerical models.

Considering the porosity formation currently can not be completely prevented, there is a need to understand the effects of the porosity in structures. With a better understanding of these effects, acceptance criteria can be derived for manufactured parts. Important research is being developed to understand the porosity effect on fatigue life, such as Wang et al. (2001) that applied statistical models to describe fatigue life due to casting defects, and Buffière et al. (2001) study microstructure and the fatigue properties of models containing artificial pores.

The damage detection research field encompasses porosity detection as well. Owolabi et al. (2003) studies damage detection in aluminium beams, Damir et al. (2007) used experimental modal analysis to quantify fatigue behavior and relate it with microstructural changes, and Yang et al. (2017) developed a Kriging model based on frequency response for damage identification.

The goal of this work is to acquire a better understanding on the effect of porosity in the natural frequency of parts. The statistical distribution of the natural frequencies are described as functions of the porosity level and spatial distribution, to be used as groundwork or reference in future detection approaches.

1.1 Objective

The main contributions of this work are:

- Numerical model based on random distributions of porosity levels and spatial distributions to study the random aspects of the associated frequency response;
- Criteria for acceptable porosity levels based on radius ranges and quantity per area;
- Influence of different porosity levels and spatial distributions in the natural frequency of an isotropic beam and an L-shaped structure.

1.2 Thesis outline

Chapter 1 provides an overall understanding and motivation for this work, as well as the objectives and the scope of the study.

In Chapter 2, an overview of the finite element method and numerical modal analysis is provided.

Chapter 3 presents the concepts of porosity and its formation process, as well as an overview of the recent studies about porosity identification methods.

A brief review with the main concepts of statistics is available in Chapter 4, where probability distributions and fit methodology are also presented.

Chapter 5 contains the porosity numerical model. Levels of porosity, distribution model, structure, finite element mesh, and the uncertainties sources are presented.

In Chapter 6, an example of probability distribution fit is shown, and the modal analysis results are discussed.

Finally in Chapter 7, the achievements from this work are presented along with suggestions for future research.

Chapter 2

Finite Element and Numerical Modal Analysis

2.1 Modal Analysis and Finite Element Background

In the following sections, the equilibrium equations and the associated finite element formulation for dynamic problems are presented in detail.

2.1.1 Elastodynamics

From the conservation of linear momentum, the balance equation in terms of stresses at a given point is

$$\boldsymbol{\nabla} \cdot \boldsymbol{\sigma} + \mathbf{b} = \rho \ddot{\mathbf{u}}, \tag{2.1.1}$$

where $\boldsymbol{\sigma}$ is the Cauchy stress tensor, $\mathbf{b}$ is the body force vector, ρ is the material density, and $\ddot{\mathbf{u}}$ the acceleration vector.

For small strains, the relation between displacement and strain is given by

$$\boldsymbol{\varepsilon} = \frac{1}{2}\left(\boldsymbol{\nabla}\mathbf{u}^T + \boldsymbol{\nabla}\mathbf{u}\right) = \mathbf{L}(\mathbf{u}), \tag{2.1.2}$$

where $\boldsymbol{\varepsilon}$ is the infinitesimal strain tensor, $\mathbf{u}$ is the displacements vector, and $\mathbf{L}(\circ)$ is a differential operator.

The isotropic linear constitutive relation, depending on the strain, can be written as

$$\boldsymbol{\sigma} = \mathbf{D} : \boldsymbol{\varepsilon}, \tag{2.1.3}$$

where $\mathbf{D}$ is the linear material constitutive tensor.

Substituting Eq. (2.1.2) in Eq. (2.1.3) and this expression in Eq. (2.1.1), it is possible to express the problem as a function of the displacement $\mathbf{u}$

$$\boldsymbol{\nabla} \cdot (\mathbf{D} : \mathbf{L}(\mathbf{u})) + \mathbf{b} = \rho \ddot{\mathbf{u}}. \tag{2.1.4}$$

To obtain the weak form of Eq. (2.1.4), an approximated vector field $\tilde{\mathbf{u}}$ is introduced, generating a residue $\mathbf{r}$ described as

$$\mathbf{r} = \boldsymbol{\nabla} \cdot (\mathbf{D} : \mathbf{L}(\tilde{\mathbf{u}})) + \mathbf{b} - \rho \ddot{\tilde{\mathbf{u}}}. \tag{2.1.5}$$

Using the inner product between the residue and a vector field, $\mathbf{w}$ (test function), weak convergence is established as

$$\int_\Omega \mathbf{w} \cdot \ \mathbf{r} \ \ d\Omega \rightharpoonup 0, \tag{2.1.6}$$

where Ω is the domain. Substituting Eq. (2.1.5) into Eq. (2.1.6) and using the distributive property of the inner product

$$\int_\Omega \mathbf{w} \cdot [\nabla \cdot (\mathbf{D} : \mathbf{L}(\tilde{\mathbf{u}}))]\, d\Omega + \int_\Omega \mathbf{w} \cdot \mathbf{b} d\Omega - \int_\Omega \mathbf{w} \cdot \rho \ddot{\tilde{\mathbf{u}}} d\Omega = 0. \tag{2.1.7}$$

Integrating the first expression of Eq. (2.1.7) by parts, results in

$$\int_\Omega \mathbf{w} \cdot [\nabla \cdot (\mathbf{D} : \mathbf{L}(\tilde{\mathbf{u}}))]\, d\Omega = \int_{\Gamma_t} \mathbf{w} \cdot \mathbf{t} d\Gamma - \int_\Omega \mathbf{L}(\mathbf{w}) : \mathbf{D} : \mathbf{L}(\tilde{\mathbf{u}})\, d\Omega, \tag{2.1.8}$$

where Γ is the boundary of Ω subjected to $\mathbf{t}$, and $\mathbf{t}$ is the vector of the forces acting in Γ_t.

The weak form is given by

$$\int_\Omega \mathbf{L}(\mathbf{w}) : \mathbf{D} : \mathbf{L}(\tilde{\mathbf{u}})\, d\Omega + \int_\Omega \mathbf{w} \cdot \rho \ddot{\tilde{\mathbf{u}}} d\Omega = \int_\Omega \mathbf{w} \cdot \mathbf{b} d\Omega + \int_\Gamma \mathbf{w} \cdot \mathbf{t} d\Gamma. \tag{2.1.9}$$

2.1.2 Finite Element Discretization

Consider a finite element e. A vector field $\tilde{\mathbf{u}}$ describes the displacements within the element via nodal discrete values $\mathbf{U}_e$ in the form

$$\tilde{\mathbf{u}} = \mathbf{N}\mathbf{U}_e, \tag{2.1.10}$$

where $\mathbf{N}$ is a matrix containing shape functions. To map the global vector $\mathbf{U}$ to its local values $\mathbf{U}_e$, an localization matrix $\mathbf{H}_e$ is used such as

$$\mathbf{U}_e = \mathbf{H}_e\mathbf{U}. \tag{2.1.11}$$

Similarly, the vector field $\mathbf{w}$ and accelerations $\ddot{\boldsymbol{u}}$ all follow the same interpolation and discretization, such that

$$\mathbf{w} = \mathbf{N}\mathbf{W}_e \tag{2.1.12}$$

and

$$\ddot{\boldsymbol{u}} = \mathbf{N}\ddot{\mathbf{U}}_e. \tag{2.1.13}$$

Using Voigt's notation and substituting the interpolation expressions in Eq. (2.1.9), results in

$$\begin{aligned}\sum_e \left(\int_{\Omega_e} \mathbf{L}_V(\mathbf{N}\mathbf{W}_e) \cdot (\mathbf{D}\mathbf{L}_V(\mathbf{N}\mathbf{U}_e))\, d\Omega_e + \int_{\Omega_e} (\mathbf{N}\mathbf{W}_e) \cdot \rho \mathbf{N}\ddot{\mathbf{U}}_e \, d\Omega_e \right) = \\ \sum_e \left(\int_{\Omega_e} (\mathbf{N}\mathbf{W}_e) \cdot \mathbf{b}\, d\Omega_e + \int_{\Gamma_e} (\mathbf{N}\mathbf{W}_e) \cdot \mathbf{t}\, d\Gamma_e \right),\end{aligned} \tag{2.1.14}$$

where Ω_e and Γ_e are the volume and boundary of an element e. The constitutive tensor $\mathbf{D}$ is now represented as a matrix and the differential operator is now $\mathbf{L}_V$ for compatibility with Voigt's notation. Now it is possible to write the inner product $\mathbf{w} \cdot \mathbf{u}$ as $\mathbf{w}^T\mathbf{u}$, such that Eq. (2.1.14) results in

$$\begin{aligned}\sum_e \left(\mathbf{W}_e^T \int_{\Omega_e} \mathbf{L}_V(\mathbf{N})^T \mathbf{D}\mathbf{L}_V(\mathbf{N})\, d\Omega_e \mathbf{U}_e + \mathbf{W}_e^T \int_{\Omega_e} \mathbf{N}^T \rho \mathbf{N}\, d\Omega_e \ddot{\mathbf{U}}_e \right) = \\ \sum_e \left(\mathbf{W}_e^T \int_{\Omega_e} \mathbf{N}^T \mathbf{b}\, d\Omega_e + \mathbf{W}_e^T \int_{\Gamma_e} \mathbf{N}^T \mathbf{t}\, d\Gamma_e \right),\end{aligned} \tag{2.1.15}$$

where it is possible to define the local matrices

$$\mathbf{K}_e = \int_{\Omega_e} \mathbf{L}_V(\mathbf{N})^T \mathbf{D}\mathbf{L}_V(\mathbf{N})\, d\Omega_e, \tag{2.1.16}$$

$$\mathbf{M}_e = \int_{\Omega_e} \mathbf{N}^T \rho \mathbf{N}\, d\Omega_e, \tag{2.1.17}$$

and

$$\mathbf{F}_e = \int_{\Gamma_e} \mathbf{N}^T \mathbf{t}\, d\Gamma_e + \int_{\Omega_e} \mathbf{N}^T \mathbf{b}\, d\Omega_e, \tag{2.1.18}$$

where $\mathbf{K}_e$ and $\mathbf{M}_e$ are respectively the stiffness and mass matrices of the element, and $\mathbf{F}_e$ is the force vector.

Simplifying Eq. (2.1.15) with the local matrices of the element and using the localization operator results in

$$\sum_e \left((\mathbf{H}_e\mathbf{W})^T \mathbf{M}_e \mathbf{H}_e \ddot{\mathbf{U}} + (\mathbf{H}_e\mathbf{W})^T \mathbf{K}_e \mathbf{H}_e \mathbf{U} \right) = \sum_e (\mathbf{H}_e\mathbf{W})^T \mathbf{F}_e, \tag{2.1.19}$$

or

$$\mathbf{W}^T\mathbf{M}\ddot{\mathbf{U}} + \mathbf{W}^T\mathbf{K}\mathbf{U} = \mathbf{W}^T\mathbf{F}, \tag{2.1.20}$$

where

$$\mathbf{M} = \sum_e \mathbf{H}_e^T\mathbf{M}_e\mathbf{H}_e, \tag{2.1.21}$$

and

$$\mathbf{K} = \sum_e \mathbf{H}_e^T\mathbf{K}_e\mathbf{H}_e, \tag{2.1.22}$$

are the mass and stiffness matrices of the global system, respectively, while

$$\mathbf{F} = \sum_e \mathbf{H}_e^T\mathbf{F}_e, \tag{2.1.23}$$

is the global force vector. Since $\mathbf{W}^T$ is present in all terms of Eq. (2.1.20), it is possible to satisfy the equilibrium equation with the following condition

$$\mathbf{W}^T\left(\mathbf{M}\ddot{\mathbf{U}} + \mathbf{K}\mathbf{U} - \mathbf{F}\right) = \mathbf{W}^T\mathbf{0}, \tag{2.1.24}$$

resulting in a global system of linear equations system in the form

$$\mathbf{M}\ddot{\mathbf{U}} + \mathbf{K}\mathbf{U} = \mathbf{F}. \tag{2.1.25}$$

2.1.3 Modal Problem

Considering that the system described by Eq. (2.1.25) does not have external forces, $\mathbf{F} = \mathbf{0}$,

$$\mathbf{M}\ddot{\mathbf{U}} + \mathbf{K}\mathbf{U} = \mathbf{0}. \tag{2.1.26}$$

The general solution for Eq. (2.1.26), subjected to non-null initial conditions, is given by

$$\mathbf{U} = \boldsymbol{\phi}e^{i\omega_n t}, \tag{2.1.27}$$

where ω_n are the natural frequencies of the system, $\boldsymbol{\phi}$ is a vector of amplitudes, known as modal vector.

Substituting Eq. (2.1.27) into Eq. (2.1.26), results in

$$\left[\mathbf{K} - \omega_n^2 \mathbf{M}\right] \left(\boldsymbol{\phi} e^{i\omega_n t}\right) = \mathbf{0}, \tag{2.1.28}$$

and knowing that $e^{i\omega_n t} \neq 0\ \forall t$, the equation (2.1.28) can be written as

$$[\mathbf{K} - \omega_n^2 \mathbf{M}]\boldsymbol{\phi} = \mathbf{0}, \tag{2.1.29}$$

that will result in a non-trivial solution, if and only if

$$\det[\mathbf{K} - \lambda \mathbf{M}] = 0, \tag{2.1.30}$$

where $\lambda = \omega_n^2$ (EWINS, 2000). Equation (2.1.30) represents a generalized eigenvalues and eigenvectors problem, with n eigenvalues λ_r, where n is the number of degrees of freedom (DOF's). Each eigenvalue has an associated eigenvector $\boldsymbol{\phi}$, corresponding to the vibration mode. The modal vectors can be grouped in a $n \times n$ matrix, or modal matrix ($\boldsymbol{\Phi}$), where each column corresponds to a vibration mode. Since $\mathbf{K}$ and $\mathbf{M}$ are symmetric and $\mathbf{M}$ is always positive-definite, all its eigenvalues are real.

2.1.4 Lumped Mass Matrix

Multiplying the general problem from Eq. (2.1.29) by $\mathbf{M}^{-1}$, the traditional eigenvalue problem is obtained:

$$[\mathbf{A} - \lambda \mathbf{I}]\,\boldsymbol{\phi} = \mathbf{0}. \tag{2.1.31}$$

This problem is easier to solve than the generalized eigenvalue problem, with the additional initial cost of inverting $\mathbf{M}$. Although there are many ways to efficiently obtain $\mathbf{A}$, for memory bounded problems like the ones studied in this work, the more efficient approach is to use a diagonal approximation to $\mathbf{M}$.

Using a lumping method, $\mathbf{M}$ is transformed into diagonal by either row or column sum lumping schemes. The method developed by Hinton et al. (1976) is applied in this work. The technique defines the values of the lumped-mass matrix proportional to the diagonal values of the consistent mass, and since the consistent mass matrix is always positive-definite, it will always produce a positive-definite lumped mass matrix (HUGHES, 2000). With a diagonal mass matrix, $\mathbf{M}_{de}$, the inversion is direct and can be stored as a vector, as

$$\mathbf{M}_{dii}^{-1} = \frac{1}{m_{ii}}. \tag{2.1.32}$$

The global mass matrix is represented by Eq. (2.1.21), $\mathbf{M_e}$ is a local consistent mass matrix and can be written as

$$\mathbf{M}_e = \int_{\Omega_e} \mathbf{N}^T \rho \mathbf{N} \, d\Omega_e, \tag{2.1.33}$$

where $\mathbf{N}$ are the shape functions the element. For a quadrilateral element,

$$\mathbf{N} = [N_1 \, N_2 \, N_3 \, N_4]. \tag{2.1.34}$$

Considering that ρ is constant in the volume Ω_e, and replacing $\mathbf{N}$ with (2.1.34),

$$\mathbf{M}_e = \int_{\Omega_e} \rho \begin{bmatrix} N_1 \\ N_2 \\ N_3 \\ N_4 \end{bmatrix} [N_1 \, N_2 \, N_3 \, N_4] \, d\Omega_e, \tag{2.1.35}$$

such that

$$\mathbf{M}_e = \int_{\Omega_e} \rho \begin{bmatrix} N_1^2 & N_1 N_2 & N_1 N_3 & N_1 N_4 \\ & N_2^2 & N_2 N_3 & N_2 N_4 \\ & & N_3^2 & N_3 N_4 \\ & & & N_4^2 \end{bmatrix} d\Omega_e. \tag{2.1.36}$$

According to Hughes (2000), $\mathbf{M}_{de}$ is obtained by diagonal scaling as

$$\mathbf{M}_{de} = \frac{\int_{\Omega_e} \rho \begin{bmatrix} N_1^2 & & & \\ & N_2^2 & & \\ & & N_3^2 & \\ & & & N_4^2 \end{bmatrix} d\Omega_e}{\mathrm{Tr}(\mathbf{M}_e)}, \tag{2.1.37}$$

where Tr is the trace.

There are many solution methods for the traditional eigenvalue and eigenvector problem, but the one chosen in this work is ARPACK (LEHOUCQ et al., 1998). The implementation is designed to compute a chosen number of eigenvalues and corresponding eigenvectors of a general $\mathbf{A}_{n \times n}$ matrix using the Implicitly Restarted Arnoldi Method

(IRAM). The Arnoldi Method returns a partial result after a small number of iterations, an advantage when compared to direct methods which must complete the process to return any result. The complexity in modal problems is proportional to the size of the **A** matrix. Higher matrix sizes will demand longer to solve the problem, as can be seen in figure 2.1, where a clear linear relation is noticed, doubling the number of elements will also almost double the execution time in the model applied in this work.

Figure 2.1 – Execution time and memory allocation × Number of elements

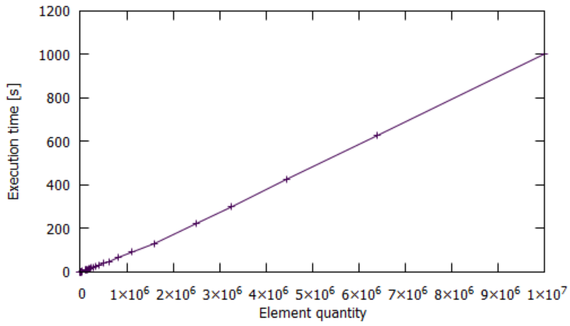

(a) Relation between execution time and the number of elements

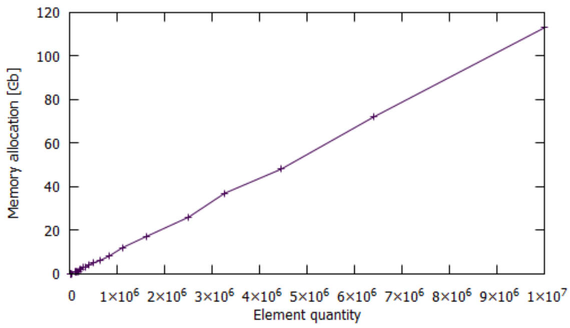

(b) Relation between memory allocation and the number of elements

Source: Author's production

Chapter 3

Porosity

All metallic components, in at least one of the phases of the manufacturing process, are submitted to fusion and solidification (LEAL, 2019).

One of the reasons for the large use of casting is its capability to manufacture components with complex geometries using materials with good mechanical characteristics. As an example, aluminium is widely used in the automotive industry since it allows for weight reduction improving performance, particularly fuel efficiency (LEE et al., 2001). According to the Brazilian Foundry Association, ABIFA, aluminium is the most used among the non-ferrous metals in Brazil, as can be seen in Figure 3.1.

Figure 3.1 – Cast production of non-ferrous metals in Brazil [10^3 t].

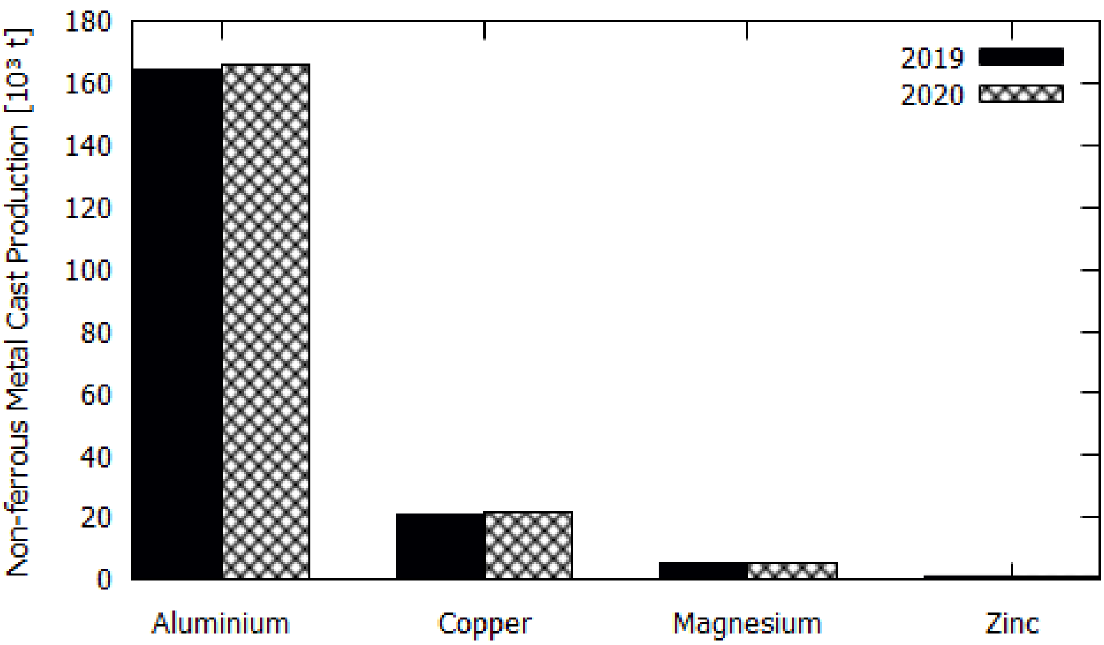

Source: Annual informative by Brazilian Foundry Association (ABIFA, 2020)

In very simple terms, the casting or foundry process consists of melting metal, pouring it into a specifically designed mold, cooling the mold until the metal solidifies, removing the mold afterward. Even though it is a process so simple that a person could perform at home for a small part, the casting of large part is a complex process. Variables such as the material, liquid pour rate, material feed regions, location and rate of cooling, and mold design all play a role in casting a good part.

A usual casting system is designed to ensure that there is a sufficient supply of additional molten material available as the casting solidifies, to fill the cavities that would otherwise form. This is known as *feeding the casting* and the reservoir that supplies the feed metal is known as a *feeder* or a *riser*. The feeder must guarantee that the feed material is liquid to satisfy the shrinkage demands of the casting and to be able to ensure a free of gross shrinkage porosity casted part (BROWN, 2000b). Figure 3.2 shows the basic components of a casting running system.

Figure 3.2 – The basic components of a casting running system.

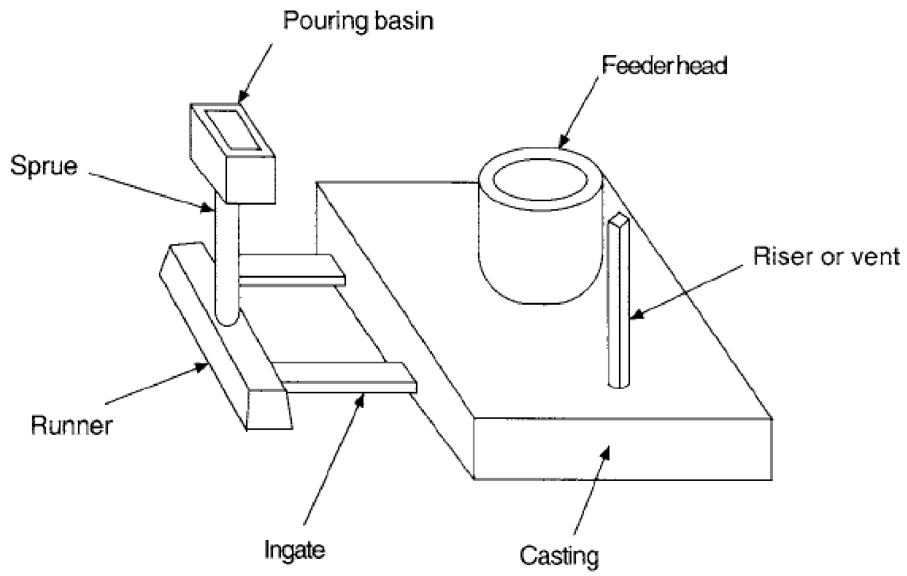

Source: Brown (2000a).

Even with an adequate casting system, many defects are present as it is a process with many variables. The most common ones are solidification shrinkage (cavity, porosity, sink), gaseous entrapment (blowholes, gas porosity), solid inclusions, and cracks from thermal contraction, to name a few. According to Sata (2010), porosity is one of the recurrent problems which impacts the quality of castings, worsening mechanical properties such as tensile strength and fatigue life.

According to Lee et al. (2001), porosity in castings can be classified by the size of the pores as macroporosity or microporosity, and also by its root cause: shrinkage porosity and gas porosity.

Shrinkage porosity is caused by regions that solidify later than their surroundings and do not have enough metal flow into the section to completely fill.

If a poorly fed region is completely cut off from a source of molten metal, then a void is formed. If the void is greater than 5 mm in length, it is designated as macroporosity (LEE et al., 2001). The area in which macro-pores form solidifies after the surrounding region, therefore, is termed as a hot spot.

If the region has an appropriate supply of liquid metal, but the feeding occurs through an area that is partially solidified, then the flow through this semi-solid region can be so restricted that the pressure is locally reduced, forming many small pores (LEE et al., 2001). Since the pores are constrained by the existing dendritic network, it assumes an irregular shape (CARLSON et al., 2002). This condition is termed as micro-shrinkage porosity'. The size of microporosity may range in length from a few microns to a few millimeters (LEE et al., 2001). Figure 3.3 shows Scanning Electron Microscopy (SEM) images of two typical pores of irregular shape.

Figure 3.3 – SEM images of two typical micro pores of irregular shape.

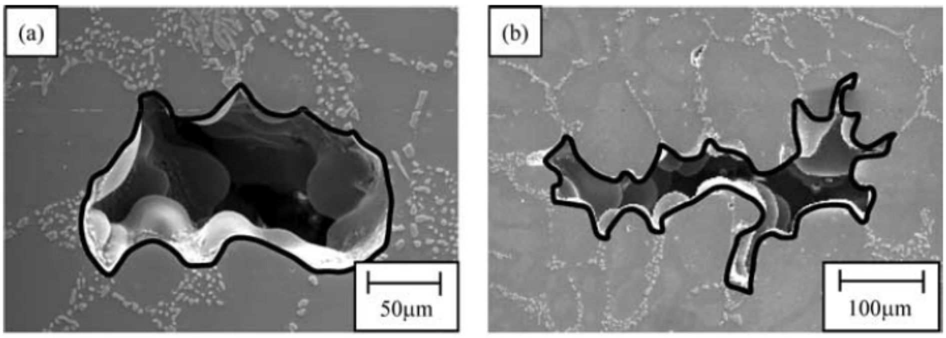

Source: Gao et al. (2004).

Gas porosity is formed since gases are less soluble in solid than in liquid metals. Thus as the metal cools and solidifies, the concentration of dissolved gases in the liquid phase increases until bubbles of gas are formed (LEE et al., 2001), usually with a spherical shape.

Another factor that influence porosity formation are changes in the direction and dimensions of liquid metal flow. A disconnection between the flux and the cavity wall may occur at these locations, generating a low-pressure region that has as consequence the aspiration of air and gas. Figure 3.4 illustrates a zone of flux shutdown, a region susceptible to porosity formation.

Porosity formation is a complex phenomenon where the sizes and distribution of pores are functions of several interacting parameters, like solubility, temperature, pressure and metallurgical composition. To fully understand and prevent porosity formation, an ideal model should be able to recreate the pore nucleation and growth by considering all the physics involved in the pore formation. Lee et al. (2001) pointed out the necessary topics that should be covered to fully recreate an ideal porosity formation model and also argues that such a model may not be industrially viable due to the complexity of the problem. Few models showing promising results are also revised, including pioneers in

Figure 3.4 – Example of flux shutdown.

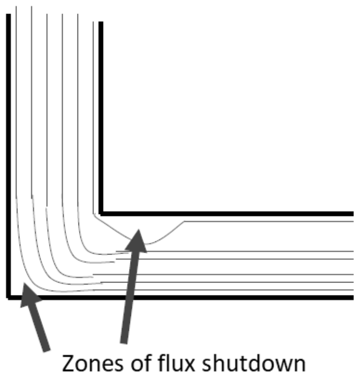

Source: Author's production.

porosity modeling as Piwonka e Flemings (1966) and Kubo e Pehlke (1985), also indicating improvements for the next generation of models.

Also, in this area of research, Carlson et al. (2002) presented a multi-phase model valid for micro and macroporosity, predicting feeding flow, melting pressure, and formation/growth of porosity in solidifying steel castings. The model is implemented in a general-purpose casting simulation code. Two cases were simulated to predict porosity distributions and compared to radiography of steel casting produced in sand molds. One of the examples tested the increase of feeding distances and the use of pressurized riser castings. For this case, two simulations were performed: a base case without pressurization and one with it. The conclusion was found that pressurizing the riser significantly reduces the amount of porosity in the casting, both in the simulation as in the experimental test. For both cases, it was shown that the porosity formation occurred in a narrow band of the centerline of the plate, as shown in Figure 3.5.

Figure 3.5 – Pore volume percentage in the middle plane, with and without pressurization.

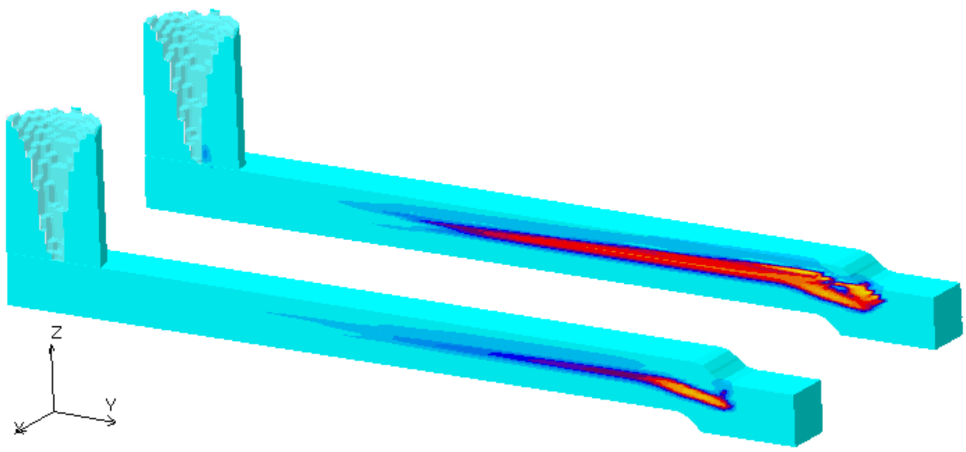

Source: Carlson et al. (2002).

The development of numerical models is still ongoing, and most of the models use a specific material, like Sabau e Viswanathan (2008) that developed a methodology for prediction of microporosity fraction in aluminium A356 alloys casting, which takes into account alloy solidification, shrinkage-driven interdendritic fluid flow, hydrogen precipitation, and porosity evolution.

Khalajzadeh e Beckermann (2020) developed a model for predicting the shrinkage porosity for Magnesium-steel alloy. The model uses the temperature and solid fraction results from a thermal simulation and predicts shrinkage porosity, including surface sinks and riser pipes, open shrinkage holes internal to the casting, and microporosity dispersed between dendrite arms.

A contribution in Khalajzadeh e Beckermann (2020) model it is based on the fact that shrinkage porosity nucleates and grows in regions where the solid fraction is the lowest. An interesting observation is that the adjustable model parameters were optimized for the Magnesium-steel and they were very similar to the ones obtained for aluminium alloy casting (KHALAJZADEH et al., 2018), indicating that the adjustable parameters may not be so sensitive to the type of alloy.

As hot spots may be predicted accurately using numerical simulation and design expertise (LEE et al., 2001), macroporosity is a defect that can be avoided. Since both shrinkage and gas driving forces contribute to the microporosity formation (Whittenberger; Rhines, 1952) and still cannot be accurately predicted, microporosities are normally present in the casting process and will be the focus of this work.

In practice, a certain amount of porosity can be tolerated in castings; however, this varies with the application. Thus it is important to identify the specific contributions of defects and other microstructural parameters on fatigue life, for example. Regarding this subject Wang et al. (2001), Avalle et al. (2002), Yi et al. (2003), Osmond et al. (2018) used samples with varying levels of porosity to perform fatigue tests. An inverse relation between pore quantity distributions and fatigue life was observed.

Wang et al. (2001) and Yi et al. (2003) used statistical models to describe the fatigue life due to casting defects. Gao et al. (2004) developed a pore-sensitive model using metallographic examination and finite element analysis to correlate fatigue life with the size of the failure-dominant pore.

3.1 Porosity Detection

Since considerable effort is being invested to quantify and predict microporosity formation and to understand the porosity effect on fatigue properties, a quantitative understanding of the role of defects in produced parts is necessary to establish defect acceptance criteria for both designs specifications as well as for quality control purposes.

A significant amount of work has been developed using modal parameters (natural frequency, modal damping, and mode shapes) for nondestructive damage detection and identification. The application of modal parameters for damage detection is attractive because, by definition, they are functions of the physical properties of the components like mass and stiffness (DAMIR et al., 2007).

The application of vibration-based techniques such as nondestructive damage identification tool, as well as in Structural Health Monitoring (SHM), is increasing.

The nondestructive damage identification tool is applied in situations where the objective is quality control, in case of castings defects or preexisting damage identification from wear. In this case, the tool is used for detection.

When the damage is detected, and the structure still has the operational capability, the SHM is applied to monitor the defect, ensuring safety during the remaining operating time. The aerospace industry is responsible for the highest payoffs in the SHM area since the equipment and structures are expensive, and damages can lead to catastrophic failures (KESSLER et al., 2002).

Tandon e Begin (1990), using modal analysis, correlated the variation in the first natural frequency with the porosity level and the presence of inclusions in a cast-steel component.

Doebling et al. (1998) presented an extensive review concerning the detection, location, and characterization of structural damage by examining changes in measured vibration response.

The distribution of internal pores of the cast model characterized by X-ray micro tomography was studied by Savelli et al. (2000). The distributions were used as input for a statistical model to calculate fatigue life distribution in cast alloys. The model presented a good agreement with experimental fatigue life at high stress.

Kessler et al. (2002) applied frequency response methods to damage detection in composite materials. A good agreement between the numerical model and experimental results was obtained between the extent of damage and the reduction in natural frequency.

A study to detect damage in aluminium beams was presented by Owolabi et al. (2003), where artificially produced cracks were made to evaluate the frequency response at different locations. A simple method to predicting the location and depth of the cracks was presented. The method is based on changes in the natural frequencies and amplitudes of the frequency response functions, and uses three vibrations modes to identify the depth and crack location.

Damir et al. (2007) used experimental modal analysis as a nondestructive tool to characterize and quantify fatigue life, which is directly impacted by changes in the microstructure.

With a different approach, Yang et al. (2017) developed a Kriging model based on frequency response for damage identification. The method was applied to a numerical example of the cantilever beam, the region with porosities was represented by elements with lower stiffness, and in an experimental setup to verify the model effectiveness.

As discussed, for some parts presence of porosity may be acceptable, but for most cases, large levels of porosity are not allowed. The concern with the lack of criteria for quality approval relating the porosity quantity with specific loadings application, like fatigue, is stated in some works. For a considerable amount of real-life applications, the quality control standard for porosity approval is based on skilled technicians know-how and the use of expensive or even destructive techniques.

A more reliable quality control system would be possible with the development and application of practical nondestructive damage identification tools. In such implementation, approval/non-approval decisions could be supported by an envelope-based model.

With this goal in mind, in the following, a study based on acceptable levels of porosity, using modal response will be presented. Random distributions of porosity level and position are numerically generated and the associated frequency responses are obtained by using the finite element method. The Monte Carlo Simulation (MCS) method is applied to obtain a statistical representation of the associated modal response and it used to assess the level of allowed porosity.

Chapter 4

Statistics

4.1 Probability

A random variable, X, is a function that assigns a real number to each outcome in the sample space, Ω, of a random experiment (MONTGOMERY; RUNGER, 2010).

If X assumes only a finite number of values, X is nominated as discrete random variable. The best example is a dice, where exists only a finite number of outcomes, $X = \{1, 2, 3, 4, 5, 6\}$.

The probability distribution of a discrete random variable is a list of probabilities associated with each of its possible values. According to Montgomery e Runger (2010), for a discrete random variable X with possible values $x_1, x_2, ..., x_n$, a probability mass function is a function such that

$$f(x_i) \geq 0 \qquad \sum_{i=1}^{n} f(x_i) = 1 \qquad f(x_i) = P(X = x_i). \tag{4.1.1}$$

The cumulative distribution function, denoted as $F(x)$, for a discrete random variable gives the probability that the variable X is less than or equal to x, for every x value, or, in other words, is the summing up of the probabilities. Even if the random variable X can only assume integer values, the cumulative distribution function can assume non-integer values (MONTGOMERY; RUNGER, 2010). For a discrete random variable, $F(x)$ must satisfies the following properties

$$\begin{cases} F(x) = P(X \leq x) = \sum_{x_i \leq x} f(x_i) \\ 0 \leq F(x) \leq 1 \\ \text{If } x_{i-1} \leq x_i, \quad \text{then } F(x_{i-1}) \leq F(x_i) \end{cases} \tag{4.1.2}$$

Two important measures are the mean and the variance, that are often used to summarize a probability distribution (MONTGOMERY; RUNGER, 2010). The expected value or mean, $E(X)$ or μ, is a measure of the center of the probability distribution

$$E(X) = \mu = \sum_x x f(x), \tag{4.1.3}$$

and the variance, σ^2 or $V(X)$, is a measure of the dispersion or variability around the mean in the distribution, defined as

$$\sigma^2 = V(X) = E(X - E(X))^2 = \sum_x (x - E(X))^2 f(x) \tag{4.1.4}$$

with standard deviation defined by

$$\sigma = \sqrt{\sigma^2}. \tag{4.1.5}$$

In practice, most variables are measurements that can vary with a tolerance range defined by an interval of real numbers. Since the number of possible values is infinite, the range of X can be thought of as continuum (MONTGOMERY; RUNGER, 2010), defining the continuous random variable.

A Probability Density Functions (PDF) $f(x)$ can be used to describe the probability distribution of a continuous random variable X. The probability that X is between a and b is determined as the integral of $f(x)$ from a to b

$$P\left(a \leq X \leq b\right) = \int_a^b f(x)\, dx, \tag{4.1.6}$$

representing the area under $f(x)$, as shown in Figure 4.1. As long as $f(x)$ is nonnegative and $\int_{-\infty}^{\infty} f(x)\, dx = 1$, then $0 \leq P(a \leq X \leq b) \leq 1$ and the probabilities are properly restricted (MONTGOMERY; RUNGER, 2010).

Figure 4.1 – Probability determined from the area under $f(x)$.

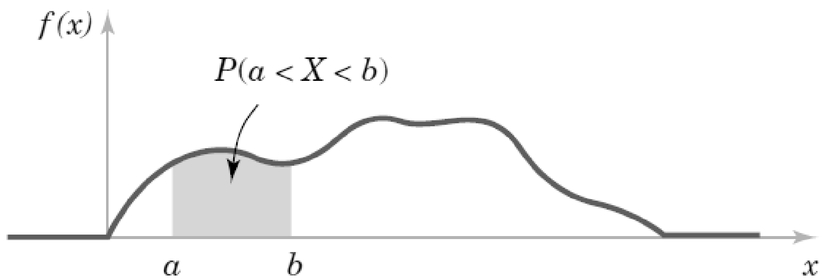

Source: Montgomery e Runger (2010).

The cumulative distribution function, CDF, on the continuum case, is given by

$$F(x) = P(X \leq x) = \int_{-\infty}^{x} f(x) dx \tag{4.1.7}$$

for $-\infty < x < \infty$.

The mean and the variance of a continuous random variable are defined similarly to a discrete random variable, with the integration replacing summation in the definitions. The mean or expected value of X, $E(X)$ or μ, is defined as

$$E(X) = \mu = \int_{-\infty}^{\infty} x f(x)\, dx, \tag{4.1.8}$$

and the variance of X, $V(X)$ or σ^2, is

$$V(X) = \sigma^2 = \int_{-\infty}^{\infty} (x - E(X))^2 f(x)\, dx, \tag{4.1.9}$$

and the standard deviation is $\sigma = \sqrt{\sigma^2}$.

The expected value and the variance are also known as the first and second moments of a statistical distribution. The moments are quantitative measures related to the shape of the probability distribution function. The third and forth moments are known as skewness and kurtosis, respectively. Skewness is a measure of the asymmetry of the probability distribution relative to the mean. A distribution skewed to the left will present a heavier tail to the left and will present negative skewness. Kurtosis defines how heavily the tails of a distribution differs from the tails of a normal distribution of the same variance. In the following, the most used probability distributions will be presented.

4.1.1 Normal Distribution

The most widely used model for the distribution of a random variable X is the Normal Distribution (MONTGOMERY; RUNGER, 2010). The normal probability density function is represented by a bell shape, where the expected value, $E(X)$, determines the center and the variance, σ^2, determines the width. The general form of its probability density function is

$$f(x) = \frac{1}{\sqrt{2\pi}\sigma} e^{\frac{-(x-\mu)^2}{2\sigma^2}} \qquad -\infty < x < \infty. \tag{4.1.10}$$

Is possible to represent the Normal Distribution with $X \sim \mathcal{N}(\mu, \sigma^2)$. It has skewness equals to 0 and kurtosis equals to 3.

As the variance is responsible for the width of the bell, it is possible to relate the amount of probability with the variance. For example, Figure 4.2 shows the area referent to different amounts of probabilities represented by the areas with 2σ, 4σ and 6σ, respective. 6σ is often referred to as normal distribution width, since 99.7% of the probability is within this interval $(\mu - 3\sigma,\ \mu + 3\sigma)$.

A normal random variable with $E(X) = 0$ and $\sigma^2 = 1$ is called a standard normal random variable and can be denoted as Z. The equation for the standard normal

Figure 4.2 – Probability determined from the area under $f(x)$.

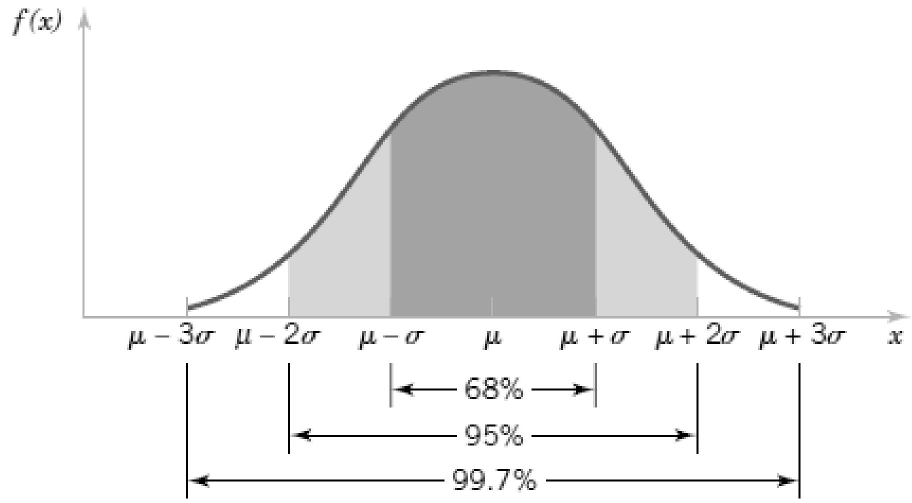

Source: Montgomery e Runger (2010).

distribution is

$$f(z) = \frac{1}{\sqrt{2\pi}} e^{\frac{-z^2}{2}}. \tag{4.1.11}$$

The cumulative distribution function of the standard normal distribution is $F(z) = P(Z \leq z)$, and can be expressed by

$$F(z) = \int_{-\infty}^{z} \frac{1}{\sqrt{2\pi}} e^{\frac{-z^2}{2}}. \tag{4.1.12}$$

As the $F(z)$ integral does not exist in a simple closed formula, it is necessary to evaluate it numerically. The typical plot for normal cumulative distribution function is shown in Figure 4.3.

A common variation of the Normal distribution is the truncation of the interval. Instead of $[-\infty, +\infty]$, it is defined according to a finite interval, such as $[a, b]$. In this case, the distribution is defined as $X \sim \mathscr{N}(\mu, \sigma^2, a, b)$.

4.1.2 Weibull Distribution

The Weibull distribution is often used to model the time until failure of many different physical systems. The parameters in the distribution provide great flexibility to model systems in which the number of failures changes with time (MONTGOMERY; RUNGER, 2010). The probability density function of a Weibull random variable is

$$f(x) = \frac{\beta}{\delta} \left(\frac{x}{\delta}\right)^{\beta-1} e^{-\left(\frac{x}{\delta}\right)^{\beta}}, \quad x > 0, \tag{4.1.13}$$

with scale parameter $\gamma > 0$ and shape parameter $\beta > 0$. Figure 4.4 shows three Weibull probability density functions for different combinations of γ and β. Shape parameter is

Figure 4.3 – Normal cumulative distribution function.

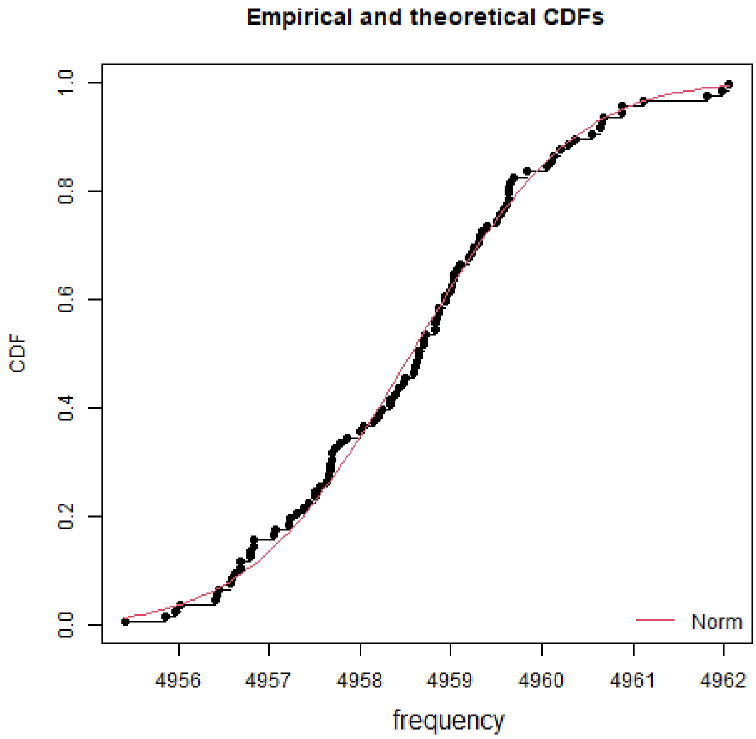

Source: Montgomery e Runger (2010).

responsible for the slope of the line in the probability plot and the scale parameter has the effect of stretching out the probability distribution function.

The Weibull cumulative distribution function of X is expressed by

$$F(x) = 1 - e^{-\frac{x}{\beta}^{\beta}}. \tag{4.1.14}$$

The expected value and the variance of a Weibull random variable X are given by

$$E(X) = \delta\Gamma\left(1 + \frac{1}{\beta}\right) \quad \text{and} \quad V(X) = \delta^2\Gamma\left(1 + \frac{2}{\beta}\right) - \delta^2\left[\Gamma\left(1 + \frac{1}{\beta}\right)\right]^2, \tag{4.1.15}$$

where Γ is the gamma function

$$\Gamma(r) = \int_0^{\infty} x^{r-1}e^{-x}dx, \quad \text{for } r > 0. \tag{4.1.16}$$

4.1.3 Log-normal Distribution

If X follows an exponential relationship like $X = exp(W)$, and W is a normal random variable, then the distribution is called a log-normal distribution. The name originates from the fact that the natural logarithm of X is normally distributed. Consid-

Figure 4.4 – Weibull probability density functions for different values of γ and β.

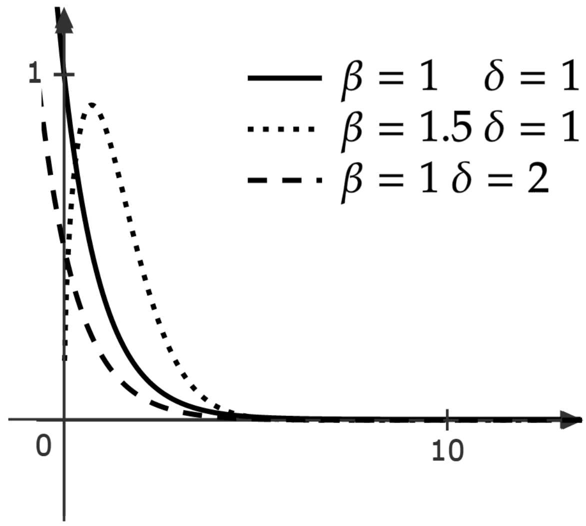

Source: Author's production.

ering that $W \sim \mathcal{N}(\theta, \omega^2)$, then the log-normal probability density function is

$$f(x) = \frac{1}{x\sigma\sqrt{2\pi}} e^{-\frac{(\ln x - \theta)^2}{2\omega^2}} \quad 0 < x < \infty, \tag{4.1.17}$$

the expected value and the variance of a log-normal distribution X are

$$E(X) = e^{\theta + \omega^2/2} \quad and \quad V(X) = e^{2\theta + \omega^2}\left(e^{\omega^2} - 1\right). \tag{4.1.18}$$

The lifetime of a product that degrades over time is often modeled by a log-normal random variable. A Weibull distribution can also be used in this type of application, however a log-normal distribution is derived from a simple exponential function of a normal random variable, so it is more easy to understand and to evaluate (MONTGOMERY; RUNGER, 2010).

4.1.4 Logistic Distribution

Logistic distribution is a continuous distribution in $\mathbb{R}$, given by $X \sim Logistic(\alpha, s)$ with $s > 0$. The logistic probability density function is

$$f(x) = \frac{e^{-\frac{x-\alpha}{s}}}{s(1 + e^{\frac{x-\alpha}{s}})^2}, \; where \quad -\infty < x < \infty \tag{4.1.19}$$

where α is the location parameter and s is scale parameter. The location parameter makes the PDF slide along X axis and the scale parameter determines how spread out the distribution is. Figure 4.5 shows three cases with different parameters combination to illustrate the parameters effect in the distribution.

The cumulative distribution function is given by

$$F(x) = \frac{1}{1+e^{\frac{x-\alpha}{s}}}, where \quad -\infty < x < \infty, \tag{4.1.20}$$

with mean $E(X)$ and variance $V(X)$ expressed by

$$E(X) = \int_{-\infty}^{\infty} \frac{xe^{-\frac{x-\alpha}{s}}}{s(1+e^{-\frac{x-alpha}{s}}}) ^2 dx, \tag{4.1.21}$$

$$V(X) = \frac{s^2\pi^2}{3}. \tag{4.1.22}$$

Figure 4.5 – Logistic probability density functions for different values of α and s.

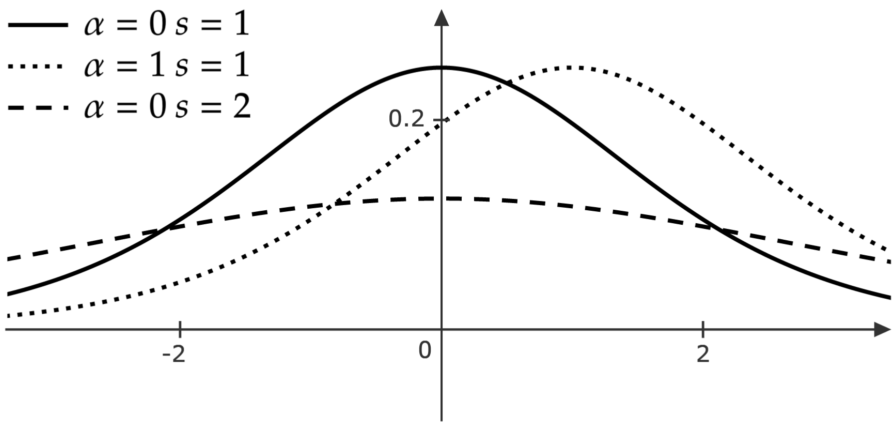

Source: Author's production.

4.1.5 Fitting Distributions

Fit a distribution consists in finding a mathematical function which represents a statistical variable. To identify the best fit to a random variable, an exploratory data analysis and graphical techniques may be necessary.

An exploratory data analysis consist in computing basic statistic from the data, as mean, standard deviation, skewness and kurtosis, to name a few. With these metrics it is possible to have an initial idea on the data behavior. Depending on the data, more information will be necessary to correctly identify the best fit.

For the graphical analysis, probability plots are used to help identify the best distribution fit for the data. In the sequence, a summary about the main graphs will be presented.

4.1.5.1 Probability Plots

The histogram provides the shape visual impression of the distribution and information about the central tendency and dispersion in the data. This display often gives insight about possible choices of probability distribution to use as a model for the population. When the sample size is large, the histogram can provide a reasonably reliable indicator of the general shape of the probability density function (MONTGOMERY; RUNGER, 2010).

Figure 4.6 – Histogram approximates a probability density function.

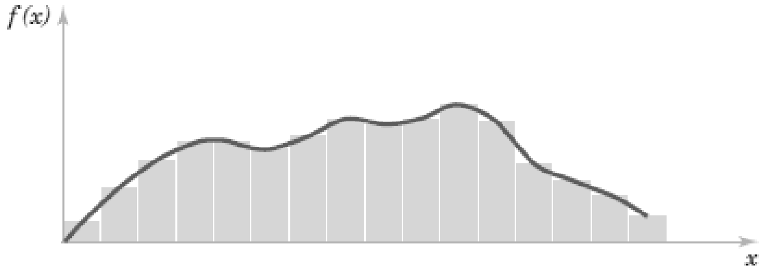

Source: Montgomery e Runger (2010).

Cullen and Frey, or skewness-kurtosis graph, use kurtosis and skewness metrics to compare the data with different distributions. The skewness and kurtosis from input data are calculated and named as an observation point. If the observation point is close to a distribution symbol, the observation model may be described by the distribution. This graph is used to help identify the distributions that could be considered in further analysis, but it is not a precise solution. In the example shown in Figure 4.7, the observation point shows that the three common right-skewed distributions could be considered: log-normal, gamma, and Weibull distributions.

A Q-Q plot, or quantile-quantile plot, is a scatter plot that is used to determine if two data sets are from populations with a common distribution by comparing the sample to the theoretical quantile. If both sets came from the same distribution, a 45° line should be formed. An example of Q-Q plot is shown in Figure 4.8.

Another graph that helps to understand the sample is the Cumulative Distribution Function (CDF) plot. The empirical CDF of sample data is compared to the theoretical CDF of a given distribution. If the values are close, the sample could be described by the evaluated distribution. Figure 4.9 shows an example of sample data acquired with the Monte Carlo Simulation method (black points) and random distributions of interest.

For the cumulative distribution function graph, the sample data is sorted in ascending order, the probability is calculated and as the points advance in the X axis, the probabilities are sum up in crescent order, creating the black points at Figure 4.9.

Aside from the plots described above, another tool used to help decide if the sample data fits a certain distribution is the goodness of fit test. The purpose is to measure the

Figure 4.7 – Cullen and Frey graph for a continuous variable.

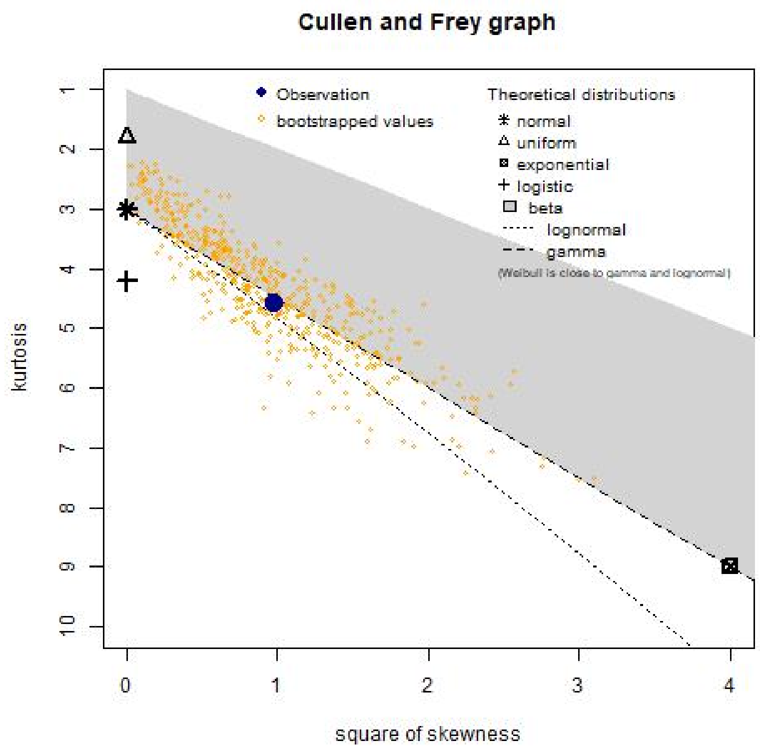

Source: Author's production.

distance between the fitted parametric distribution and the empirical distribution. The most used goodness of fit tests are the chi-square, which is the oldest goodness of fit test dating back to Karl Person in 1990, Kolmogorov-Smirnov, Anderson-Darling, and Shapiro-Wilk (THODE, 2011). The main difference between the tests The tests usually follow a hypothesis test, with null, H_0, and alternative hypothesis, H_a, where:

- H_0: The data follow a specified distribution;
- H_a: The data do not follow the specified distribution.

H_0 is accepted if the test p-value is greater than the significance level of at least 5%.

If p-value is smaller than a significance level of 5%, it is possible to affirm that the sample data don't occur due mere chance and can be discarded with statistically significance.

To decide the best fit for distribution, an analysis considering an interpretation of all methods shown above is ideal. When data is fitted, part of the information can be lost since it will hardly be a perfect match with a proposed distribution.

The goodness of fit test is used to reject distributions candidates, and the probability plots provide visual support to define the best fit for the data. When the goodness of fit test presents a p-value higher than the significance level for candidates with symmetric and non-symmetric distributions, knowing what the data represents can help to

Figure 4.8 – Q-Q plot example.

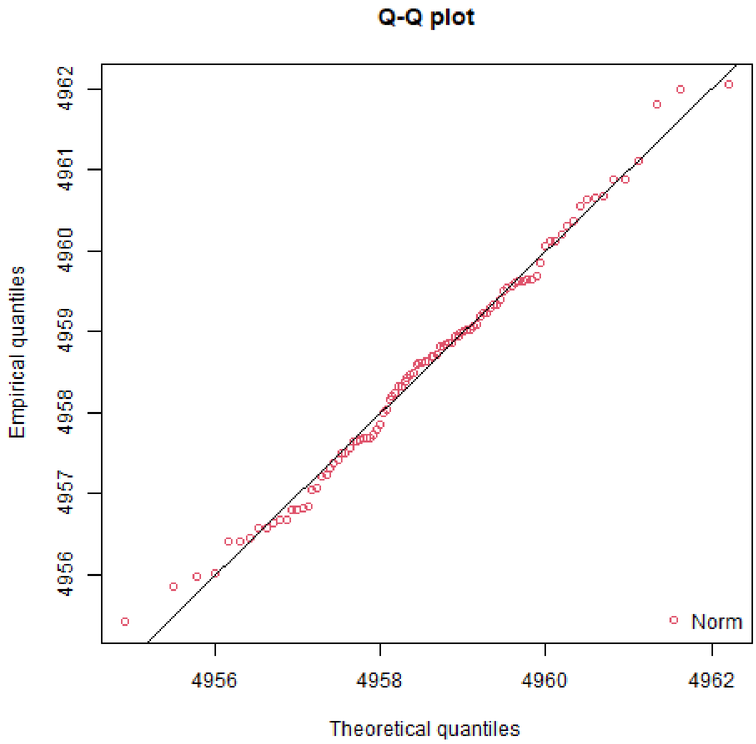

Source: Author's production.

choose the best distribution fit. For example, for the lifetime of a product, it is expected a non-symmetric distribution, so the Weibull or the log-normal distribution would be more appropriate than the Normal distribution.

A wrong distribution choice can lead to serious consequences, like a wrong specification of time lead to a process line or wrong engineering design resulting in damage of expensive equipment. The probability plots will support the decision since it supplies comparisons between theoretical and empirical data, and also provides information about the data shape.

In Chapter 6, a practical example of distribution fit will be fully discussed.

4.1.6 Monte Carlo Simulation

In real-life applications, some characteristics will likely deviate from the design values. Since variations are expected, these must be accounted for to achieve a robust design. When it is possible to map the random variables with significant impact in the design phase, simulations to predict the output behavior can be performed and techniques such as the Monte Carlo Simulation (MCS) (NEWMAN; BARKEMA, 1999) method can be applied.

By using a large number of realizations, the MCS method is capable to generate

Figure 4.9 – Example of a CDF graph.

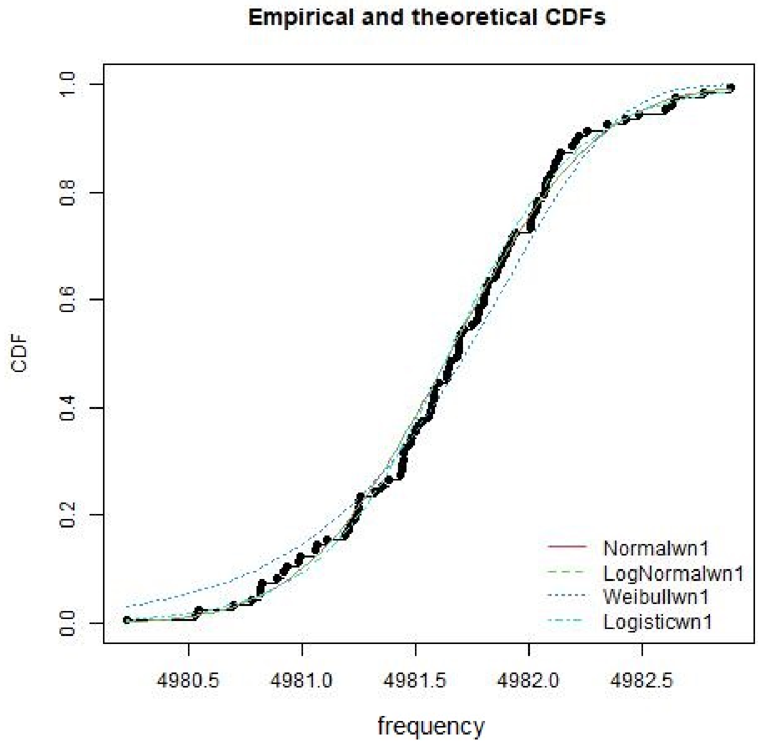

Source: Author's production.

N random scenarios using random input variables from the desired model, simulate the model for each scenario, and acquire an output vector, with all N responses. With the output vector it is possible to fit the response into a probability distribution, which can be used to better understand the impact of the input variations on the output response.

The number of input variables depends on each application, and it will influence the MCS method response as more scenarios (realizations) will be necessary to accurately capture their characteristics. To have a reliable output model, the range of all input variations need to be fully covered.

Figure 4.10 shows an MCS example. This specific example use a function with two input variables, $F(\beta, \sigma)$. Let $n \in [1, N]$ where N is the number of simulations. β and σ are random and independent variables that vary according to known random distributions, Φ and Ψ, respectively. F is solved at every realization n with new inputs that were randomly generated from Φ and Ψ, resulting in an output, $F(\beta_n, \sigma_n) \rightarrow \delta_n$. Using the output vector, $\boldsymbol{\delta}$, it is possible to fit the output behavior into some probability distribution, Ω. With this probability distribution, better understanding of the process is achieved, allowing to better represent process variations. This example assumes that the input and the output follow normal probability distributions.

The better option for the output probability distribution can be defined using the fitting parameters discussed in the previous sections.

Figure 4.10 – MCS scheme.

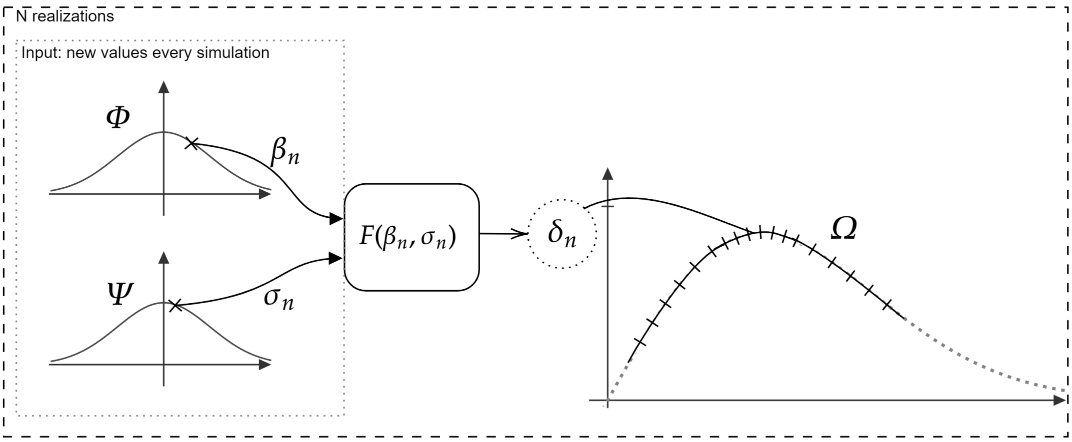

Source: Author's production.

Chapter 5

Porosity Numerical Model

5.1 Porosity Levels Definition

The ASTM E505 standard provides reference radiography images that categorize and determine the severity levels of discontinuities that may occur in aluminium and magnesium alloy die castings. *Category A* represents porosity defects, which vary from Grade 1 (Best) to Grade 4 (Worst) porosity quantity. It is stated that the acceptance criteria can be specified based on radiography and particular requirements.

Avalle et al. (2002) applied the ASTM E505 to study three batches with different levels of porosity: reference material, Grade 2, and 4 (Category A). Figure 5.1 shows representative surfaces for the three batches.

Figure 5.1 – Porosity distribution for the reference material, Grade 2 and Grade 4.

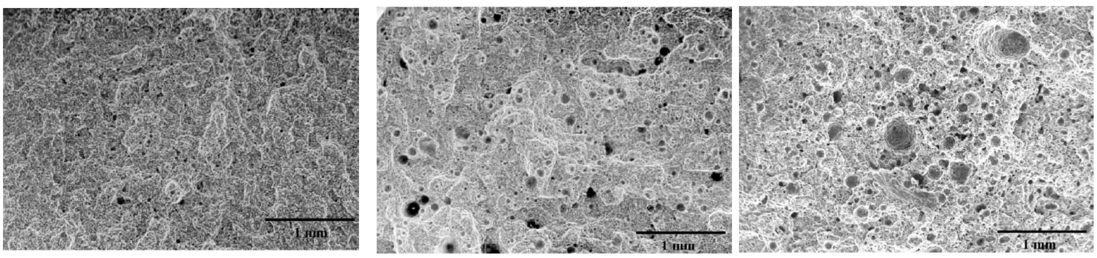

(a) Reference Material (b) Grade 2 (c) Grade 4

Source: Avalle et al. (2002).

To generate the porosity model applied in this work, the image for the reference material (Figure 5.1(a)) was used as a basis to derive a simple correlation in order to determine the quantity and diameter of the porosities. In the area of the picture area, approximately $1 \times 10^{-5} m^2$, 19 porosities were identified and separated into three radius ranges. The chosen porosities used in this work are only for a numeric academic example. Particular applications may need specific data. Table 5.1 shows the quantity of porosity for each radius range. Figure 5.2 highlights the porosities that were considered for the distribution, rR_1 - diamond / rR_2 - triangle / rR_3 - circle.

Figure 5.2 – Porosities used to determine acceptable distribution.

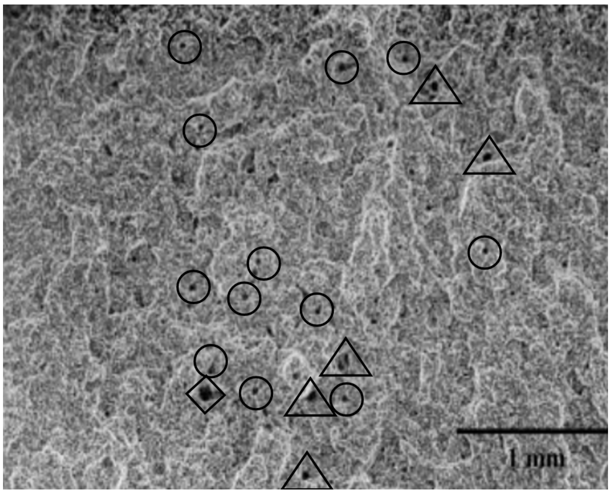

Source: Author's production.

Table 5.1 – Porosity distribution reference.

Radius Range	Porosity quantity - nP	$R_{Min}[\times 10^{-5}\,m]$	$R_{Max}[\times 10^{-5}\,m]$
rR_1	1	4.0	6.0
rR_2	6	2.5	4.0
rR_3	12	1.8	2.5

5.1.1 Porosity Distribution Model

To represent the porosity in the finite element model, it is necessary to define the porosity space, pS, which represents the region where porosity is considered, shown as the gray structure in Figure 5.3. With the porosity space defined, it is possible to establish the acceptable amount of porosity for the space area using the porosity quantity defined in Table 5.1.

The porosity center, pC, is randomly defined inside the porosity space, pS, and it is always coincident with an element center, $pC \in U[1, Nel_{pS}]$, where U is an uniform distribution and Nel_{pS} is the total number of elements inside the porosity space.

The porosity radius, pR, is then randomly generated from a specific truncated normal distribution for each radius range, $pR \sim \mathcal{N}(0, 1, R_{Min}, R_{Max})$.

Since the casting pores have an irregular shape, they were idealized as circumferences to simplify the numerical model. A similar consideration was assumed by Gao et al. (2004). The center of all elements contained within the porosity radius are identified and stored in a vector, $\mathbf{E_d}$, represented by the black circles at Figure 5.3.

The elements in $\mathbf{E_d}$ have their mass and stiffness values multiplied by a small number x_e to artificially represent voids. This weighting is conducted during the global mass and stiffness matrix assembly. Using the global stiffness matrix to exemplify this

Figure 5.3 – Porosity generation method.

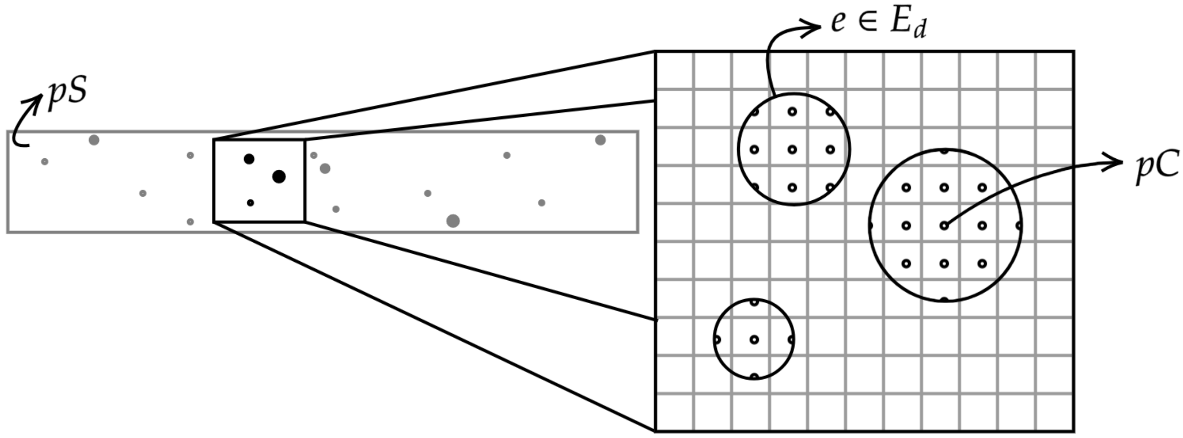

Source: Author's production.

step, where e is the element,

$$\mathbf{K} = \sum_e \mathbf{H}_e^T x_e \mathbf{K}_e \mathbf{H}_e, \tag{5.1.1}$$

where

$$x_e = \begin{cases} 1 & \rightarrow \quad e \notin E_d \\ 1 \times 10^{-8} & \rightarrow \quad e \in E_d \end{cases}. \tag{5.1.2}$$

Depending on the porosity distribution, spurious vibration modes may appear. Their origin is due to the high mass-to-stiffness ratio generated by the parameterization of Eq. (5.1.2). Similar behavior is found on topology optimization problems ((MONTERO, 2019), (PEDERSEN, 2000)). The spurious modes are manually evaluated and discarded in this work.

A very refined finite element mesh is needed to properly represent the porosities, due to their small radius. For example, for the porosity sizes considered in this work, finite elements as small as $1 \times 10^{-5} m$ are required to properly model the voids. Thus, although it may not be a challenge concerning the processing capabilities needed to obtain a small number of eigenvalues, it is a problem concerning memory requirements. For example, 90 out of the 126Gb of available RAM were used, which in turn allowed for no parallelism. Also, as a very large number of elements is used ($nel_{beam} = 1 \times 10^7$), there is no need to use fancy finite element formulations to obtain a good description of the modal response. The numerical model considers plane stress and the four-node quadrilateral isoparametric element for the mesh.

Mesh tests were performed to verify the representation capacity of different porosity diameters. The element size of $1 \times 10^{-5} m$ presented distinction between the ranges and was the element size used. The number of elements required to represent the radius range is presented in Table 5.2.

In a simplified way, the porosity distribution is created by the following steps:

Table 5.2 – Number of necessary elements to represent the porosity range.

	Element quantity	
Range	Min	Max
rR_1	49	109
rR_2	21	45
rR_3	9	21

Source: Author's production.

- Define the porosity space (area), pS;
- Define the porosity quantity proportional to the porosity space, nP;
- Randomly define the porosity center inside the porosity space, $pC \sim U(1, Nel_{pS})$;
- Porosities radius randomly generated by a truncated normal distribution, $pR \sim \mathscr{N}(0, 1, R_{Min}, R_{Max})$;
- Identify and store the elements contained within the porosities, E_d;
- Assembly $\mathbf{K}$ and $\mathbf{M}$ global matrices allocating the porosity-elements;
- Perform modal analysis and extract natural frequencies.

Figure 5.4 shows three porosity distributions examples generated by the above algorithm, following the proportions present in Table 5.1.

Figure 5.4 – Three porosity distribution generated by numerical model - Area equivalent to $1 \times 10^{-5} m^2$.

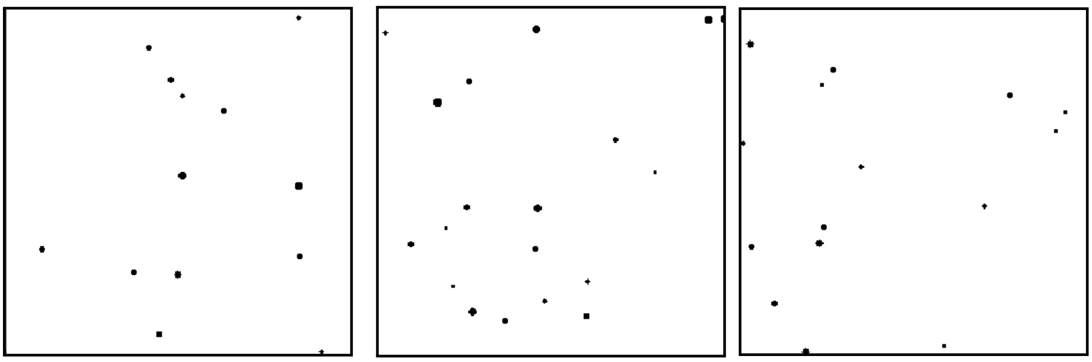

(a) (b) (c)

Source: Author's production.

5.1.2 Structure and mesh information

Six different setups are used to evaluate the modal response due to the presence of porosity.

A beam is used for initial evaluations since it is a simple geometry with well-known mode shapes. Two fixation methods are used with a total of four porosities spaces, resulting in five simulations setups.

An L-shaped domain is used to verify a more complex structure behavior. A single fixation method with one porosity space is simulated, resulting in one simulation setup.

A summary of the cases is presented in Table 5.3, and Figure 5.5 illustrates all structures with the respective porosity spaces in black.

Table 5.3 – Simulations summary.

	Structure	Fixation method	Porosity space pS	Figure reference
beamFfAll	Beam	Free-free	All beam	5.5(a)
beamFfExtX	Beam	Free-free	External extremities along X axis	5.5(b)
beamFfLmX	Beam	Free-free	Along neutral line	5.5(c)
beamFixfAll	Beam	Fixed-free	All beam	5.5(a)
beamFixfExtY	Beam	Fixed-free	Fixed extremity along Y axis	5.5(d)
bootFfCenter	L-shaped	Free-free	Center corner	5.5(e)

Source: Author's production.

Simulation cases with different porosity domains (beamFfExtX, beamFfLmX, beamFixfExtY, LshapedFfCenter) were chosen to observe the influence of the porosity formation region on the natural frequency as stated in Chapter 3, there are regions with a higher chance of porosity nucleation. Table 5.4 presents the beam, L-shape and porosity spaces dimensions. With the intention of creating a model capable of capturing the effect

Table 5.4 – Beam, L-shape and porosity spaces dimensions.

	L	H	L_1	h_1	h_2	S_1	S_2	S_3	S_4
Dimension [m]	0.1	0.01	0.02	0.002	0.001	0.05	0.05	0.01	0.01

Source: Author's production.

of porosity level and distribution on the modal response, six cases of porosity quantity were defined for the beam.

Using the porosity distribution reference defined at Table 5.1, a proportion was set for the case beamFfAll as accepTable, $pQ4$. From the acceptable case, other five cases were defined where three cases have less porosity, representing an acceptable porosity level; and two are defined with non-accepTable porosity amounts. Table 5.5 presents the porosity quantity cases used for the simulations set ups beamFfAll and beamFixfAll.

For the cases, beamFfExtX, beamFfLmX, beamFixfExtY, the porosity space area, A_{pS}, are the same: $A_{Ps} = 0.2A_t$, where A_t is the total beam area. Since the porosity level is proportional to the area, the porosity quantity cases will be reduced by $0.2\times$,

Figure 5.5 – Structures, dimensions and porosity space (regions in black) for the simulations set ups.

(a) Set up used for bFFall and bFixFall.

(b) Porosity space used for bFFextX.

(c) Porosity space used for bFFextX.

(d) Porosity space used for bFixFextY.

(e) Porosity space used for LshapedFfCenter.

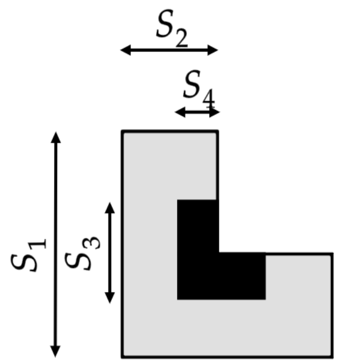

Source: Author's production.

as described in Table 5.6. The case $pQ10$ presents an acceptable amount of porosity, equivalent to $pQ4$.

Considering the L-shaped as a more complex structure than the beam, the same evaluation was performed to observe if the natural frequency behavior would be similar. The only difference between the L-shape and the beam was regarding the number of elements. To represent all L-shaped areas with the same element size, the dimensions should be $S_1 = S_2 = 0.01m$. Since this would result in a very small part, the solution was to use a refined central region, while the remaining area has progressively increasing element sizes. The L-shape area with this approach is $S_1 = S_2 = 0.05m$. The highlighted region in Figure 5.6 represents the homogeneous refined elements and the maximum element size is $e_{ext} = 2.25 \times 10^{-5}m$. This model has $nel_{Lshape} = 9.72 \times 10^6$.

Even knowing that large numbers of realizations provide better accuracy results with the MCS method, as the number of beam simulations cases is elevated and each simulation takes nearly $30min$, the amount of 100 realizations showed good convergence

Table 5.5 – Porosity quantity cases for simulations set ups beamFfAll and beamFixfAll.

Radius Range [$10^{-5}\,m$]		Porosity quantity - nP					
R_{Min}	R_{Max}	$pQ1$	$pQ2$	$pQ3$	$pQ4$	$pQ5$	$pQ6$
4.0	6.0	8	50	83	100	116	133
2.5	4.0	50	300	500	600	700	800
1.8	2.5	100	600	1000	1200	1400	1600

Source: Author's production.

Table 5.6 – Porosity quantity cases for simulations set ups beamFfExtX, beamFfLmX and beamFixfExtY.

Radius Range [$10^{-5}\,m$]		Porosity quantity - nP					
R_{Min}	R_{Max}	$pQ7$ -	$pQ8$	$pQ9$	$pQ10$	$pQ11$	$pQ12$
4.0	6.0	2	10	17	20	23	27
2.5	4.0	10	60	100	120	140	160
1.8	2.5	20	120	200	240	280	320

Source: Author's production.

for the mean and standard deviation. It was the number of realizations used for all beam cases.

As for the L-shaped, more realizations were necessary for convergence, so the porosity quantity cases were reduced to three, and the realizations quantity was prioritized. Mean convergence was almost achieved with 650 realizations, however more simulations were needed if time allowed. Figure A.6 shows the convergence evolution for the first natural frequency from the cases beamFfAll and LshapedFfCenter. All convergence graphs are available in Appendix A.

The L-shape porosity quantity cases are shown at Table 5.7. Case $pQ14$ represents the acceptable amount of porosity.

Table 5.7 – Porosity quantity cases for simulation set up LshapedFfCenter.

Radius Range [$10^{-5}\,m$]		Porosity quantity - nP		
R_{Min}	R_{Max}	$pQ13$	$pQ14$	$pQ15$
4.0	6.0	1	7	10
2.5	4.0	4	44	59
1.8	2.5	7	88	117

Source: Author's production.

For all the simulations the material used was alluminium. The material properties are shown in Table 5.8.

Figure 5.6 – L-shaped mesh.

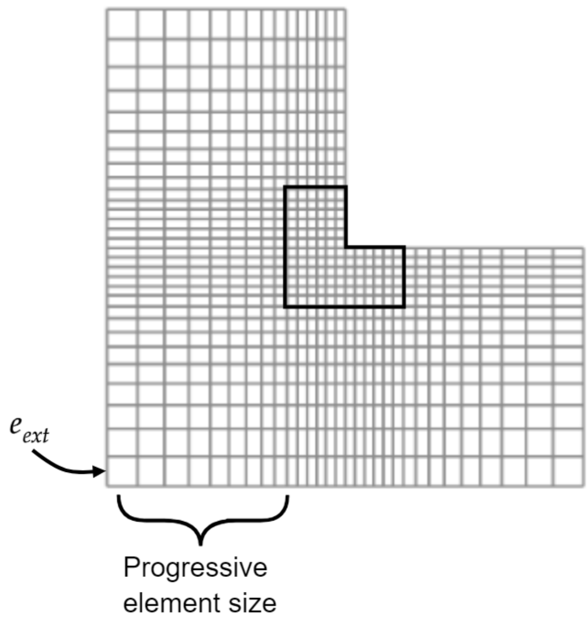

Source: Author's production.

Table 5.8 – Beam material properties.

Material	Aluminium
Density [kg/m³]	2700.0
Elastic [GPa]	68.0
Poisson's ratio	0.33

Source: Author's production.

5.2 Other Uncertainties Sources

Other factors than the porosity are also random and can influence the random response of the natural frequencies. For example, fixation methods like clamped are modeled as perfect in finite elements but are far from perfect in experimental setups. Also, dimensional variances can influence the modal response, and damping can deviate from the resonances obtained experimentally from the natural frequencies obtained from the numerical model.

Thus, it is important to understand and to quantify their influences in the random modal response in addition to the influence of the porosity.

5.2.1 Fixation method

When using a correlation model generated with data from numerical simulation, a model adjustment is necessary to consider the differences between the numerical and the experimental setup.

An example is the fixed-free fixation method. A perfect fixation would be represented in the numerical model, but in the experimental set up would be very difficult to recreate the perfect fixation, since the fixation rigidity would be different, generating changes in the measured frequencies. A common way to adjust the numerical model is to change the perfect fixation for calibrated rigidity springs to achieve desirable values natural frequencies.

If the problem allows, this uncertainty can be eliminated with free-free fixation method, since it does not present fixation stiffness. Thus the most used fixation method for experimental modal analysis.

As this work only addresses the numerical part, any fixation method is accepTable, but in order to verify whether the fixation method influences on the porosity distribution model modal response, both methods were simulated.

5.2.2 Damping

All materials possess a certain amount of internal damping, which is manifested as dissipation of energy under vibration, Jeary (1997). In modal analysis, the damping in an experimental setup represent a decay of value of the natural frequency, ω_n, generating the damped frequency, ω_d, and the relation between the two is described as

$$\omega_d = \omega_n \sqrt{1 - \zeta^2}, \tag{5.2.3}$$

where ζ is the damping ratio.

As the damping ratio is associated with the experimental setup and with the material, the presence of internal porosity can influence the damping ratio and, consequently, the damped frequency show unexpected variations impairing the comparison with the numerical model.

Alva e Desai (2006) estimated the damping ratio of aluminium manufactured through the powder metallurgy process and compare it with commercially available cast aluminium. The damping ratio was determined by sweep sine test using the half-power bandwidth method. Table 5.9 show both damping ratios. Alva e Desai (2006) commented

Table 5.9 – Damping ratios for cast and sintered Al beams.

	Cast Al	Sintered Al
ζ	0.0025	0.0040

Source: Alva e Desai (2006).

Table 5.10 – Damping influence on natural frequency.

	ω_{n1}	std	%
porosity influence	4958.560	1.422	0.029%
damping influence	4958.520	0.040	0.0008%

Source: Author's production.

that the reason for the increased value in to the sintered specimen could be due the voids and pores' presence incorporated during the powder metallurgy process. In the article, it is shown that the sintered specimen presents porosity in the range of $5\mu m$, similar to the acceptable material reference from Avalle et al. (2002). The sintered damping ratio will be used as a parameter for the acceptable state and the cast damping ratio will be used for the free porosity state.

Considering that the natural frequency will be reduced by 0.0008% due to the sintered damping ratio of 0.0040, the reduction is smaller than the standard deviation found in the numeric simulation for the case with acceptable amount of porosity for material reference, Table 5.10. This means that a measured damped frequency with an acceptable amount of porosity still would be respecting the range inside the standard deviation for the natural frequency, not causing a wrong interpretation of the result.

5.2.3 Dimensional Variation

Independent of the manufacturing process, dimensional variation will always be present, but the allowed tolerances will depend on the final application. Usually, the tolerances are defined by the size and manufacturing process. For cast components, the casting method will heavily influence the final tolerance. For example, sand casting consist of a method with sand mold that has worst finish than die casting, which consist of a method with steel/metal mold.

In regard to the tolerances, if nothing is specified in the project, the tolerances will follow normative standards, as an example, NADCA (2015). Two categories for die casting tolerances are presented: standard and precision.

As the dimensions may vary, for the frequency variation with porosity presence model, it is important to know the impact of this variation at the measured frequency.

A beam natural frequencies can be estimated using the equation

$$\omega_n = (\beta)^2\sqrt{\frac{EI}{\rho A}} = (\beta l)^2\sqrt{\frac{EI}{\rho A l^4}}, \tag{5.2.4}$$

where E is Young modulus, I is moment of inertia, ρ is density, A is cross section area,

β is a constant depending on boundary conditions, and l is the beam length. In chapter 8, Rao e Fah (2011) presented a relation of βl for most common boundary conditions for the transverse vibration mode of a beam.

Considering a beam with a rectangular section with thickness b and height h, it is possible to express the natural frequencies as a function of the dimensions h and l,

$$\omega_n = (\beta l)^2 \sqrt{\frac{Eh^2}{12\rho l^4}}, \tag{5.2.5}$$

Assuming the beam will respect the proportion $l = 10h$, than it is possible to have an natural frequency equation depending only at inverse of the beam length,

$$\omega_n = (\beta l)^2 \sqrt{\frac{0.01E}{12\rho l^2}} = \frac{1}{l}(\beta l)^2 \sqrt{\frac{E}{1200\rho}}. \tag{5.2.6}$$

The natural frequency can be represented as a length tolerances function,

$$\omega_n(\delta l) = \begin{cases} \overline{\omega_n} & = l^- \\ \underline{\omega_n} & = l^+ \end{cases} \tag{5.2.7}$$

where l^- is the lower admissible value and l^+ is the maximum admissible value for the length. Thus, the range of frequencies is $[\underline{\omega_n}, \overline{\omega_n}]$, and it is possible to relate both uncertainties.

Table 5.11 presents the tolerances for linear dimensions for aluminium casting from NADCA (2015) are presented. E_1 is illustrated at Figure 5.7.

Considering a beam with $l = 0.1m$, the l variation according to standard tolerance from Table 5.11 will be $\pm 0.325\%$, generating a frequency variation of $\pm 0.325\%$. For the precision tolerance, the frequency variation is $\pm 0.125\%$. Since the only property variation in the beam is due to the length, the frequency variation is proportional.

The frequency variation is the same as the dimension because in this case, the only variation came from the length. When the proportion $l = 10h$ is not respected, the natural frequency will be represented as a length and height tolerance function,

$$\omega_n(\delta l, \delta h) = \begin{cases} \overline{\omega_n} & = l^-, h^+ \\ \underline{\omega_n} & = l^+, h^- \end{cases}. \tag{5.2.8}$$

Table 5.11 – Tolerances for linear dimensions for aluminium castings.

	Casting Aluminium	
Length of dimension E_1	Standard tolerance	Precision tolerance
Basic tolerance up to 1" (25.4mm)	±0.010 (±0.25mm)	±0.002 (±0.05mm)
Additional tolerance for each additional inch over1" (25.4mm)	±0.001 (±0.025mm)	±0.001 (±0.025mm)

Source: NADCA (2015).

Figure 5.7 – Linear dimensions $E1$.

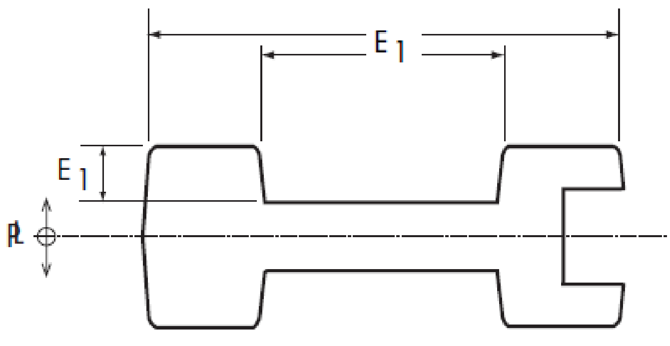

Source: NADCA (2015).

Chapter 6

Results

In this chapter, the results obtained from the fit probability distribution methodology and modal analysis with porosity distributions cases are presented. The first section discusses the distribution fit technique, the second and third sections will present the beam and the L-shape results, respectively.

6.1 Probability distribution fit

Considering the MCS scheme shown in Figure 6.1, it is possible to visualize the global simulation process. Φ is a uniform distribution, where $pC \in U(1, Nel_{pS})$ with Nel_{pS} being the total number of elements inside the porosity space. Ψ_1, Ψ_2, Ψ_3 are truncated normal distributions that generate porosity radius from range pR_1, pR_2 and pR_3, respectively. With the input random variables generated, the modal analysis, F, is evaluated and the first four natural frequencies, ω_n, stored. The first modes were evaluated because they are the smaller frequency values, so it is easier to measure experimentally, and showed good percentual of variation for the evaluated porosity cases.

For the beam cases, 100 realizations, N, were performed for each porosity quantity case presented in Table 5.5 and 5.6.

To understand the behavior of each natural frequency, a probability distribution is fitted for every natural frequency from each case, represented by Ω, Υ, ψ and φ in Figure 6.1.

The distribution fit for porosity quantity case $pQ4$ with beamFfAll for ω_{n1}, as for all other cases, was performed using probability plots and goodness of fit test. All probability plots and tests were performed using R packages.

The Cullen and Frey graph is used to have a spatial idea of the position of kurtosis and skewness among various probability distribution candidates, Figure 6.2. The observation references the sample data and it is close to normal, lognormal, gamma, and Weibull distributions, being good candidates to represent the data. Shapiro-Wilk goodness of fit

Figure 6.1 – MCS scheme used for evaluate porosity distribution.

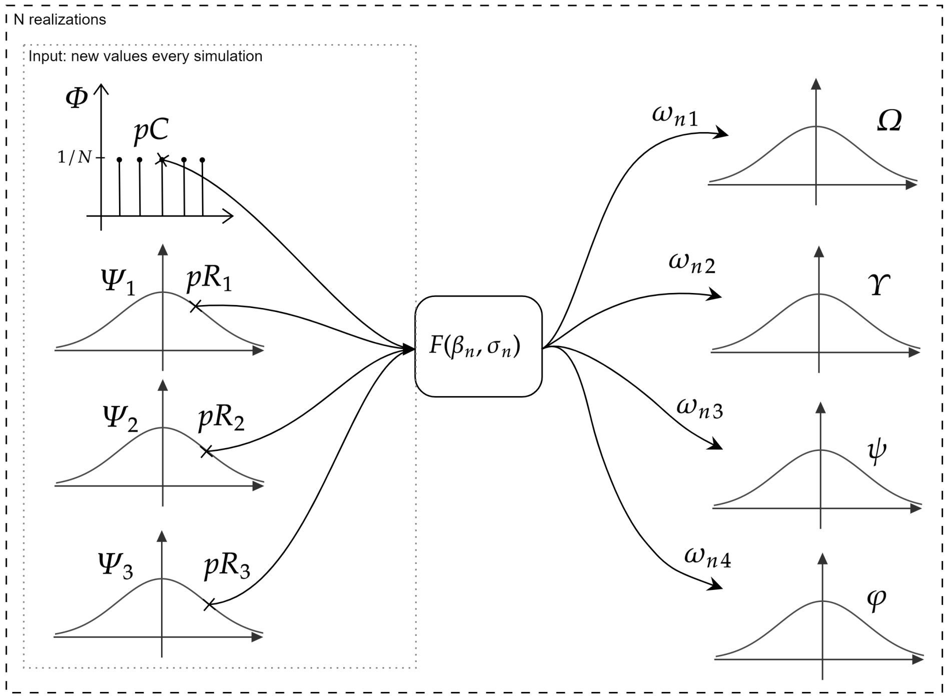

Source: Author's production.

Table 6.1 – Shapiro-Wilk goodness of fit test for case 4 - ω_{n1} - beamFfAll.

	p-value
norm	0.613112
Weibull	9.87E-05
lnorm	0.614084
logis	0.274878

Source: Author's production.

test is performed to eliminate distribution candidates. Table 6.1 shows the p-value results for ω_{n1}. With the p-value it is possible to perform the hypothesis test, where:

- H_0: The data follow a specified distribution;
- H_a: The data does not follow the specified distribution.

H_0 is accepted for normal, lognormal, and logistic distributions since the p-value is bigger than 5%. For the Weibull distribution, the H_0 is not accepted, since the p-value is smaller than the significance value of 5%.

The cumulative distribution plot and Q-Q plots help to visualize how the sample data behaves in relation to the theoretical distributions.

For the following Figures (6.3, 6.5, and 6.4) the normal, log-normal, Weibull, and logistic distributions will be considered.

Figure 6.2 – Cullen and Frey graph for case 4 - ω_{n1} - beamFfAll.

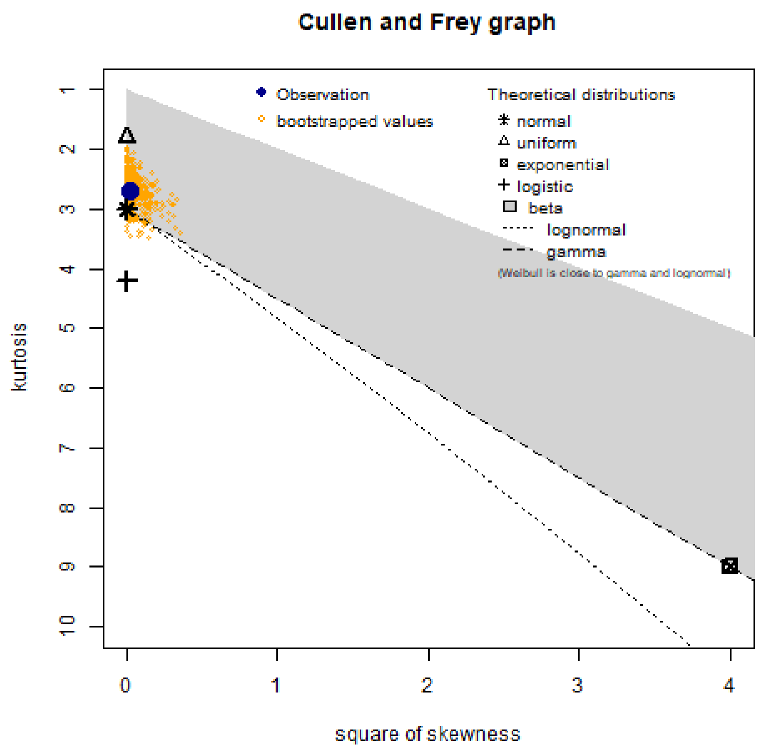

Source: Author's production.

The black points at CDF graph, Figure 6.3, represent the cumulative probability from the sample data, and for the most part, it is similar to normal, log-normal, and logistic distributions.

The Weibull distribution shows similar cumulative distribution at the intervals $[0.2-0.5]$ and $[0.8-1.0]$. In the others parts, the distribution does not represent the sample data cumulative distribution.

The Q-Q plot, normal, logistic, and lognormal distributions follow the black reference line in almost all extensions, deviating a little at the extremities. The Weibull distribution has significant deviation in the lower extremity and a little in the middle region.

Comparing the sample data histogram with the theoretical densities, in Figure 6.5, the Weibull distribution is left-skewed and misses a significant part of the data on the right side. Normal, lognormal, and logistic distributions shown good data representation, with logistic presenting more density in the middle and less on both sides.

Evaluating all probability plots and the goodness of fit test, it is possible to exclude the Weibull distribution since it presented a p-value inferior to the significant value of 5%, shown significant deviation on the CDF and Q-Q plot, and does not properly represent the data when comparing with the histogram.

The logistic distribution is not a good fit for the data, while the p-value for it is

Figure 6.3 – Cumulative distributions for beamFfAll $pQ4$ - ω_{n1}.

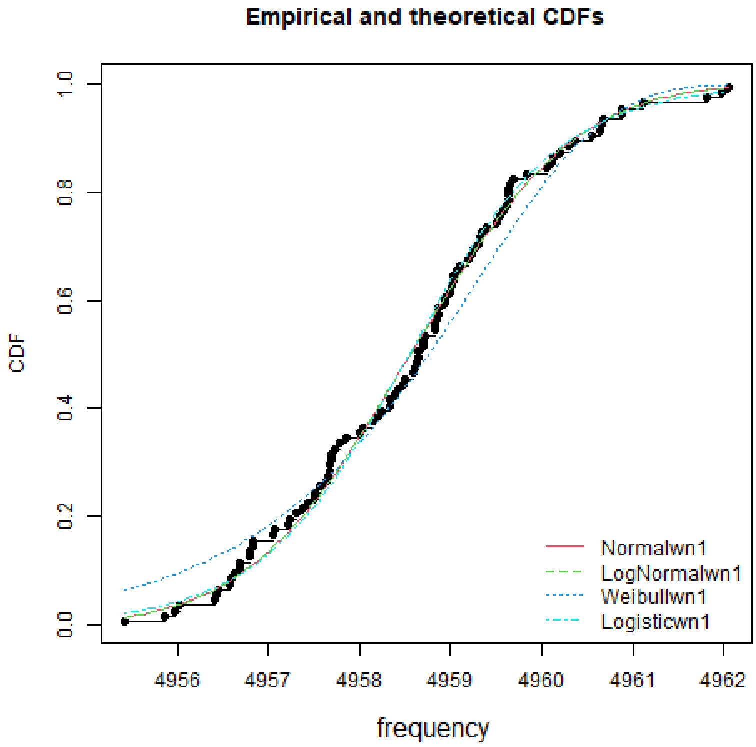

Source: Author's production.

significant and the sample data shows good compatibility in the CDF and Q-Q plot, the distributions have larger density closer to the mean when evaluating the histogram.

Normal and log-normal distributions present significant p-value, and are a good representation of the data in the CDF, Q-Q plot, and histogram. Each one of them could be chosen to represent the sample data, but the normal distribution is chosen.

This process was reproduced for all beam cases, resulting in 120 probabilities distributions. The distributions are shown in Table 6.2. As each porosity setup generate a different frequency response on the structure, different distributions will better represent the frequency response. The densities from the probability distributions shown in the following subsection, present in the natural frequency behavior graphs, were increased by a factor to improve visualization.

Table 6.2 – Fitted distributions for beam cases.

		ω_{n1}	ω_{n2}	ω_{n3}	ω_{n4}
beamFfAll	pQ1	norm	weibull	weibull	weibull
	pQ2	logistic	logistic	logistic	logistic
	pQ3	norm	logistic	logistic	weibull
	pQ4	norm	logistic	norm	norm
	pQ5	norm	lnorm	norm	logistic
	pQ6	norm	norm	norm	logistic
beamFfExtX	pQ7	logistic	norm	logistic	norm
	pQ8	norm	logistic	norm	norm
	pQ9	norm	logistic	logistic	norm
	pQ10	norm	norm	norm	norm
	pQ11	logistic	norm	norm	norm
	pQ12	norm	norm	norm	norm
beamFfLmX	pQ7	norm	norm	norm	norm
	pQ8	logistic	norm	norm	norm
	pQ9	norm	norm	norm	norm
	pQ10	norm	norm	norm	norm
	pQ11	norm	logistic	norm	norm
	pQ12	norm	norm	norm	norm
beamFixfAll	pQ1	logistic	weibull	norm	weibull
	pQ2	norm	logistic	norm	norm
	pQ3	logistic	norm	norm	norm
	pQ4	norm	logistic	norm	norm
	pQ5	norm	norm	logistic	norm
	pQ6	norm	norm	weibull	norm
beamFixfExtY	pQ7	logistic	weibull	norm	weibull
	pQ8	norm	norm	norm	norm
	pQ9	norm	norm	norm	weibull
	pQ10	norm	logistic	norm	logistic
	pQ11	norm	logistic	norm	logistic
	pQ12	norm	logistic	norm	norm

Source: Author's production.

Figure 6.4 – Q-Q plot for case 4 - ω_{n1} - beamFfAll.

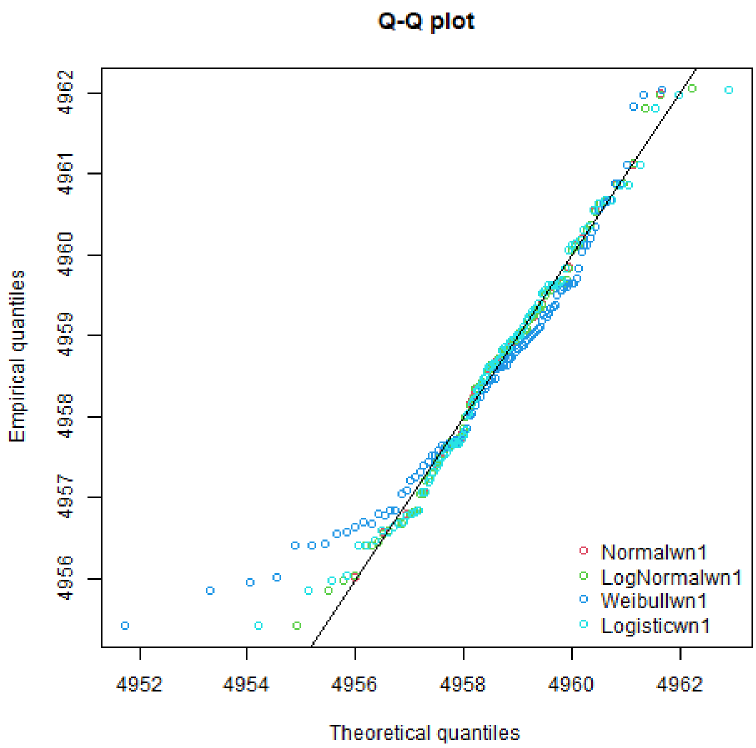

Source: Author's production.

Figure 6.5 – Histogram and theoretical densities for case 4 - ω_{n1} - beamFfAll.

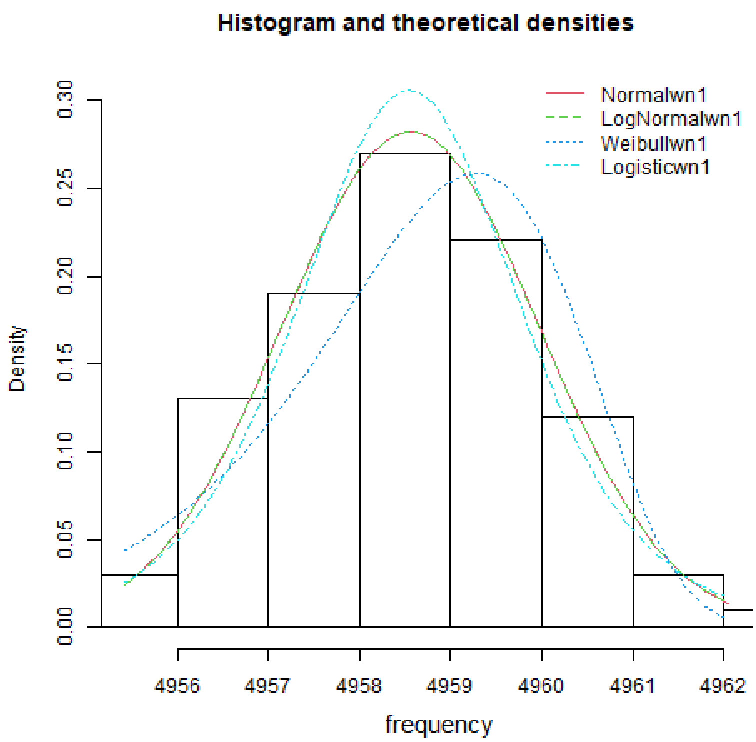

Source: Author's production.

6.2 Beam modal analysis

With the probability distributions defined, it is possible to evaluate the behavior of the natural frequency for each case.

The four vibration modes that were observed are presented in Figure 6.6 for the free-free beam and in Figure 6.7 for the fixed-free beam. The modes are from a free of porosity state. Natural frequency data for all simulated cases are presented in Table 6.3.

For the cases that follow a normal probability distribution, it is possible to affirm that 68% of the cases ω_{n1} will be inside the range of $[\mu(\omega) - \sigma(\omega); \mu(\omega) + \sigma(\omega)]$, where $\mu(\omega)$ is the natural frequency mean and $\sigma(\omega)$ is the natural frequency standard deviation.

Natural frequency decays as porosity quantity increases for the four modes in beamFfAll (Figure 6.11), beamFfExtX (Figure 6.9), beamFixfAll (Figure 6.11) and beamFixfExtY (Figure 6.12).

The reduction in frequency is expected since the porosity can be interpreted as material loss and stiffness reduction. This behavior was also observed by Tandon e Begin (1990), Kessler et al. (2002), and Owolabi et al. (2003) in experimental modal analysis cases.

An interesting point is that the same behavior is observed for the beam cases subjected to similar porosity distributions but with different fixation methods, free-free and fixed-free (beamFfAll and beamFixfAll). This shows that the effect of porosity in the natural frequency is independent of the fixation method. This information can be useful for an application where it is not possible to use a free-free fixation method. For an experimental situation, a numerical model adjustment still needs to be performed.

For the Free-Free beam (beamFfAll), a natural frequency decay of 0.5% still met the acceptance criteria for porosity levels defined in Section 5.1. Table 6.4 shows the frequency percentage reduction from the porosity-free state to the porosity acceptable

Figure 6.6 – Free-free beam vibration modes.

(a) First vibration mode.

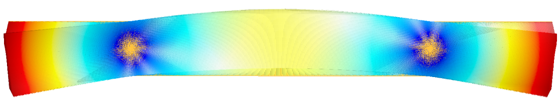

(b) Second vibration mode.

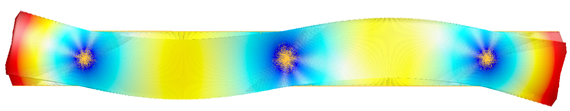

(c) Third vibration mode.

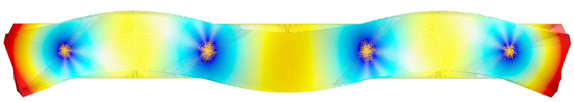

(d) Fourth vibration mode.

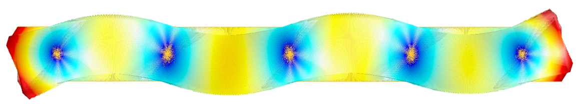

Source: Author's production.

Table 6.3 – Mean ω for the beam test cases [Hz].

		ω_{n1}	ω_{n2}	ω_{n3}	ω_{n4}
beamFfAll	0	4983.723	12972.904	23685.184	36177.947
	pQ1	4981.650	12967.464	23675.351	36162.907
	pQ2	4971.207	12940.588	23626.112	36088.278
	pQ3	4962.974	12918.928	23586.311	36028.124
	pQ4	4958.560	12907.418	23565.995	35996.896
	pQ5	4954.476	12897.370	23547.651	35968.478
	pQ6	4950.481	12886.635	23527.192	35939.071
beamFfExtX	pQ7	4982.457	12969.834	23679.878	36170.738
	pQ8	4976.160	12954.547	23654.540	36135.641
	pQ9	4971.033	12942.466	23633.860	36106.518
	pQ10	4968.798	12936.219	23623.710	36091.967
	pQ11	4966.343	12930.295	23613.963	36077.690
	pQ12	4963.494	12923.958	23603.632	36064.456
beamFfLmX	pQ7	4983.850	12973.004	23684.995	36177.060
	pQ8	4984.475	12973.733	23684.186	36173.106
	pQ9	4985.008	12974.266	23683.642	36169.442
	pQ10	4985.228	12974.472	23683.281	36167.988
	pQ11	4985.506	12974.854	23682.999	36166.260
	pQ12	4985.785	12975.047	23682.889	36164.364
beamFixfAll	0	805.303	4827.729	12705.910	23069.584
	pQ1	804.959	4825.674	12700.500	23059.667
	pQ2	803.310	4815.794	12674.521	23012.716
	pQ3	801.921	4807.801	12653.734	22975.101
	pQ4	801.301	4803.627	12642.716	22955.288
	pQ5	800.643	4799.864	12632.936	22936.971
	pQ6	799.950	4795.609	12621.621	22915.916
beamFixfExtY	pQ7	804.998	4826.889	12704.459	23067.166
	pQ8	803.524	4822.727	12697.084	23054.880
	pQ9	802.372	4819.486	12691.224	23044.997
	pQ10	801.818	4818.020	12688.711	23040.754
	pQ11	801.222	4816.275	12685.628	23035.774
	pQ12	800.633	4814.565	12682.485	23030.545

Source: Author's production.

Figure 6.7 – Fixed-free beam vibration modes.

(a) First vibration mode. (b) Second vibration mode.

(c) Third vibration mode. (d) Fourth vibration mode.

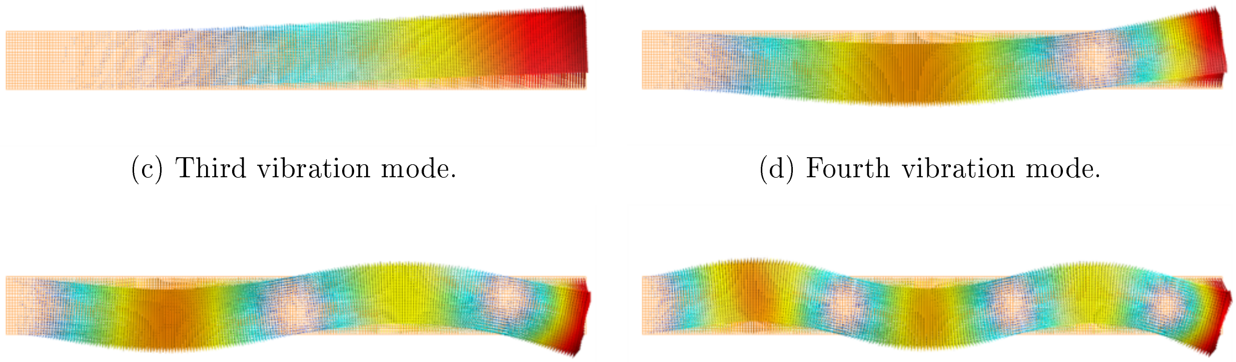

Source: Author's production.

Table 6.4 – Beam natural frequency percentage reduction - free porosity / acceptable porosity state.

	ω_{n1}	ω_{n2}	ω_{n3}	ω_{n4}
beamFfAll	0.505%	0.505%	0.503%	0.500%
beamFfExtX	0.299%	0.283%	0.260%	0.238%
beamFfLmX	-0.030%	-0.012%	0.008%	0.028%
beamFixfAll	0.497%	0.499%	0.497%	0.495%
beamFixfExtY	0.433%	0.201%	0.135%	0.125%

Source: Author's production.

state - point d in the graphs. As discussed above, beamFfAll case presented a similar percentage reduction in relation to the beamFixfAll. The porosity distribution for the case beamFfLmX, Figure 6.10, does not show significant influence on bending modes, as the natural frequencies shown a small variation in relation to other porosity cases, Table 6.4. An evaluation on the axial modes could lead to a better porosity identification for this setup.

As the porosities were placed only in the neutral plane, the porosity effect is not transmitted to the natural frequency. This effect can be interpreted in a way that only natural frequency measures would not detect neutral plane porosities, maybe a combination of modal parameters, as damping variations with unchanged vibration modes, could lead to a porosity identification in the neutral line. On the other hand, the neutral plane of a beam is usually not heavily loaded and could tolerate high concentrations of porosity compared with other locations.

The beamFixfExtY and beamFfExtX, both show frequency decay with the increased porosity presence.

beamFixfExtY shows a bigger percentage reduction for the first natural frequency

Figure 6.8 – Natural frequency behavior with increase porosity quantity - beamFfAll.

(a) Natural frequency ω_{n1} × Porosity quantity

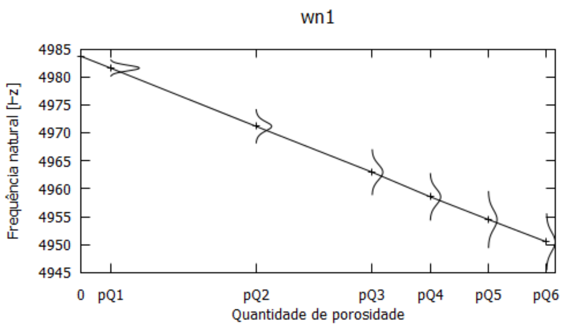

(b) Natural frequency ω_{n2} × Porosity quantity

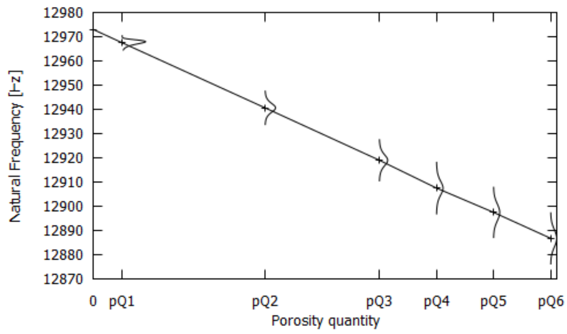

(c) Natural frequency ω_{n3} × Porosity quantity

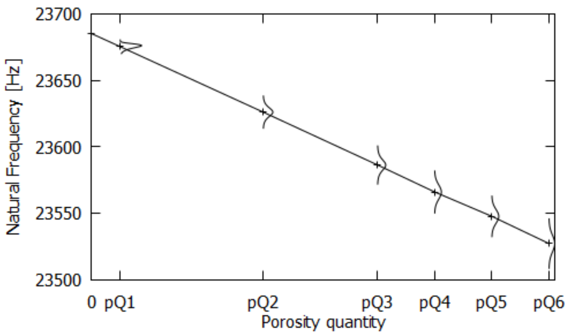

(d) Natural frequency ω_{n4} × Porosity quantity

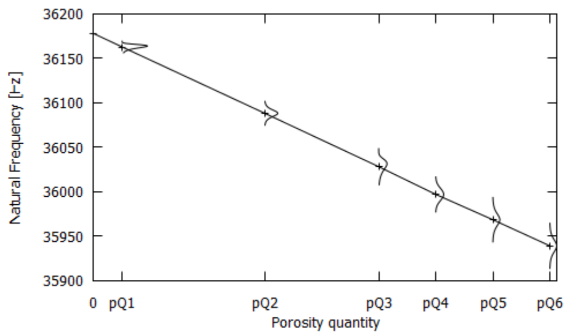

Source: Author's production.

when compared with beamFfExtX. beamFixfExtY also has smaller frequency decay for higher frequencies. This demonstrates a first vibration mode sensitivity for porosity presence in the fixed region. This pattern of bigger reduction in the first natural frequency, with little effect in higher frequencies, can represent porosity presence in the fixation region.

As for the beamFfExtX case, the frequency percentage variation is constant for higher vibration modes. A constant reduction at the first four natural frequencies can represent porosity presence in the extremities along X axis.

To differentiate beamFfAll from beamFfExtX, since both cases show a constant frequency reduction within the different vibration modes, the pattern could be based on the reduction amount, since for the case beamFfAll the reductions are more significant. Care is needed with this conclusion since a percentage reduction of 0.5% for beamFfExtX would mean non-acceptable levels of porosity.

As for the probability distributions, for the cases beamFfAll, beamFfExtX, beamFfExtX, and beamFixfExtY, it is possible to affirm that for 68% of the cases a good distinction between the porosity quantity cases will be effective.

Figure 6.9 – Natural frequency behavior with increase porosity quantity - beamFfExtX.

(a) Natural frequency ω_{n1} × Porosity quantity

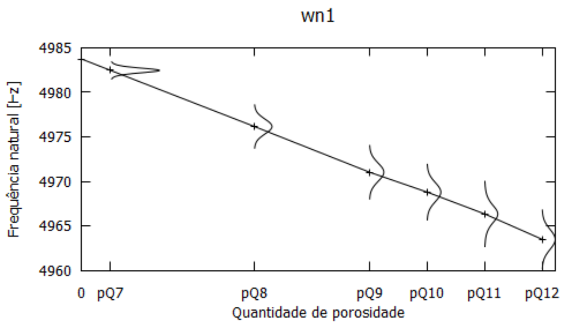

(b) Natural frequency ω_{n2} × Porosity quantity

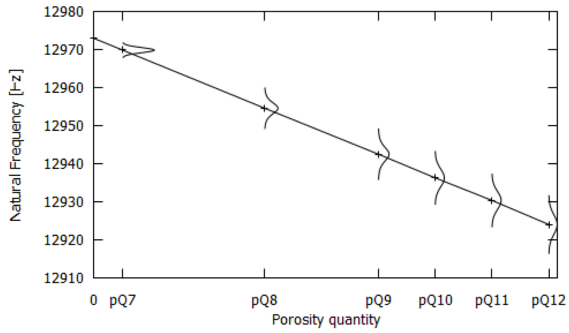

(c) Natural frequency ω_{n3} × Porosity quantity

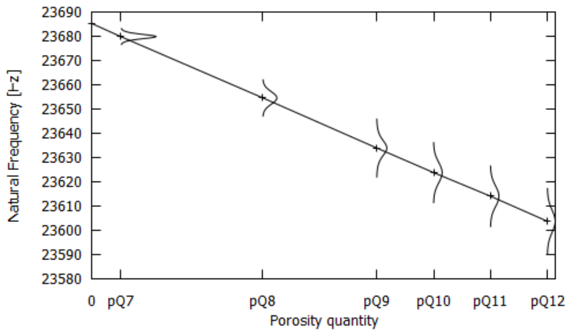

(d) Natural frequency ω_{n4} × Porosity quantity

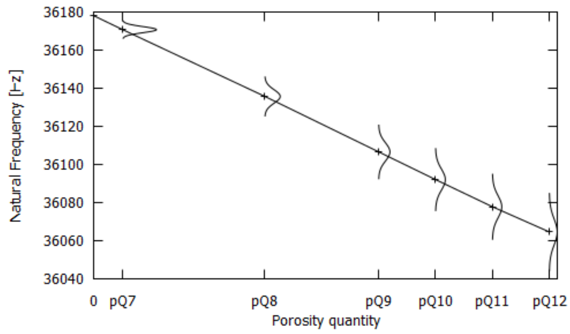

Source: Author's production.

Figure 6.10 – Natural frequency behavior with increase porosity quantity - beamFfLmX.

(a) Natural frequency ω_{n1} × Porosity quantity

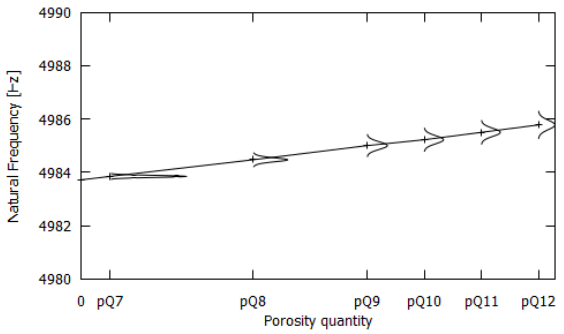

(b) Natural frequency ω_{n2} × Porosity quantity

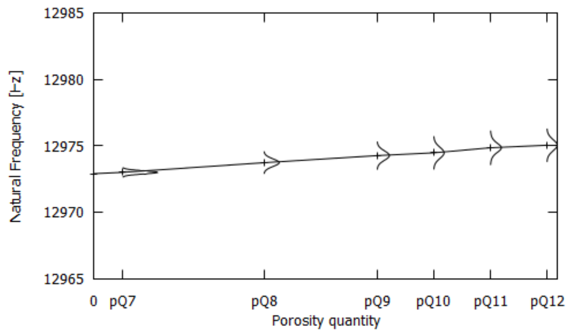

(c) Natural frequency ω_{n3} × Porosity quantity

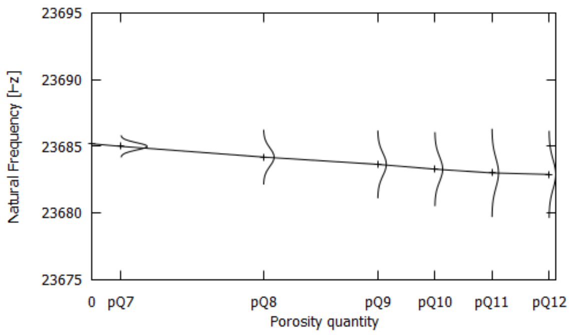

(d) Natural frequency ω_{n4} × Porosity quantity

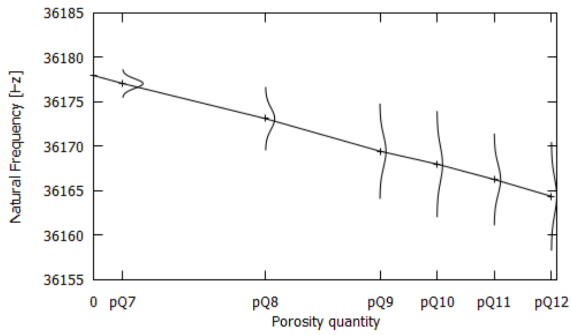

Source: Author's production.

Figure 6.11 – Natural frequency behavior with increase porosity quantity - beamFixfAll.

(a) Natural frequency ω_{n1} × Porosity quantity

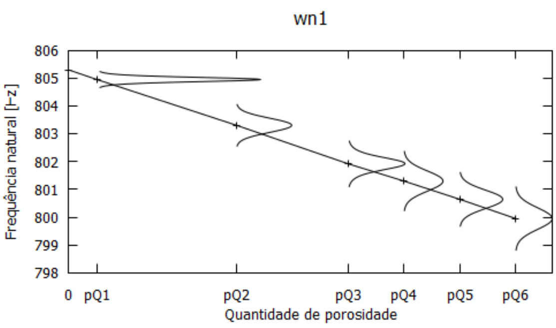

(b) Natural frequency ω_{n2} × Porosity quantity

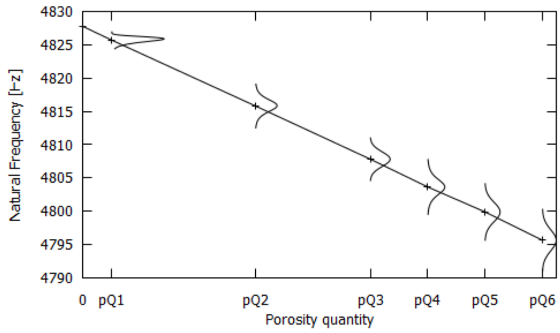

(c) Natural frequency ω_{n3} × Porosity quantity

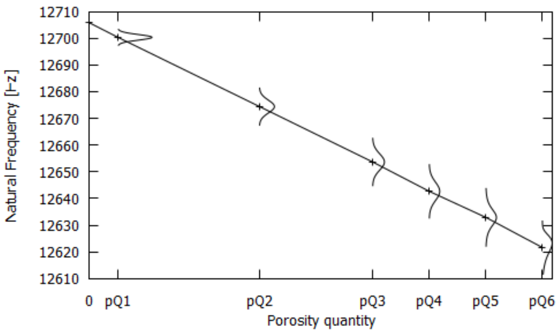

(d) Natural frequency ω_{n4} × Porosity quantity

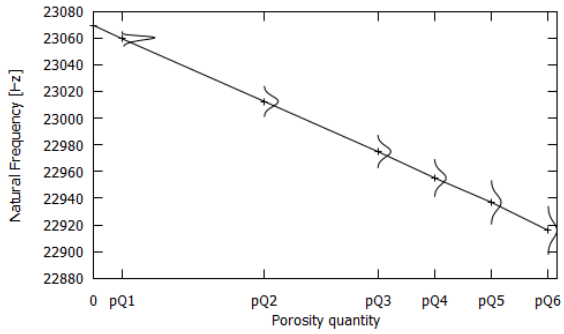

Source: Author's production.

Figure 6.12 – Natural frequency behavior with increase porosity quantity - beamFixfExtY.

(a) Natural frequency ω_{n1} x Porosity quantity

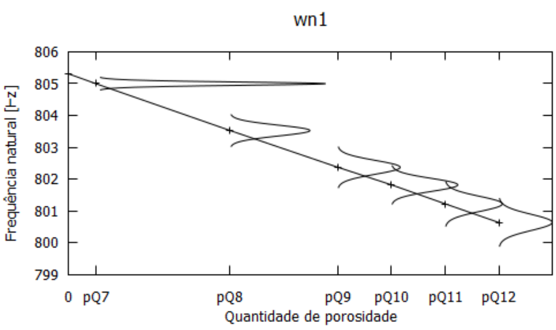

(b) Natural frequency ω_{n2} x Porosity quantity

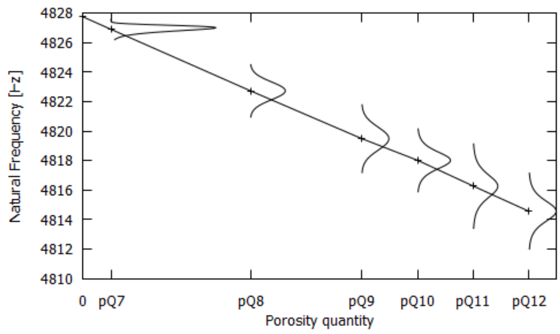

(c) Natural frequency ω_{n3} x Porosity quantity

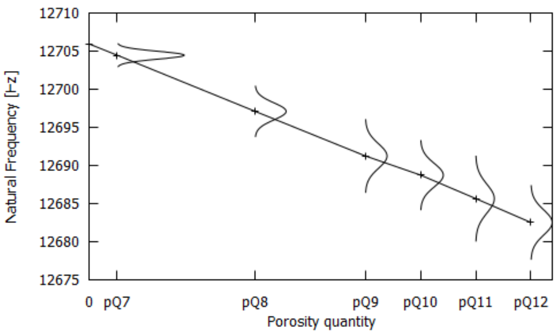

(d) Natural frequency ω_{n4} x Porosity quantity

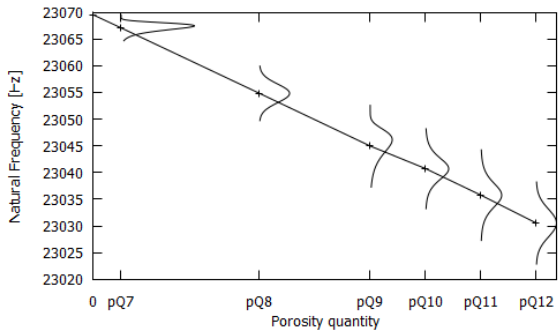

Source: Author's production.

6.3 L-shape modal analysis

As the L-shaped geometry is a small structure, it presents elevated natural frequency values, so standard deviations have a bigger scale than the ones from the beam simulations. Even with 650 realizations, the mean and standard deviation did not achieve satisfactory convergence. As the porosities do not have any constraint with respect to the location in the L-shaped domain, the number of allowed combinations is far superior from the beam, impacting the natural frequency variations thus, more realizations are needed to properly describe the distribution.

Figure 6.13 shows natural frequency behavior with porosity increase for the first four vibrations modes, Figure 6.14. Column η_f represents the mean porosity fraction for each case. In Table 6.5 the fitted probability distributions are presented.

Table 6.5 – Fitted distributions for L-shaped cases.

		ω_{n1}	ω_{n2}	ω_{n3}	ω_{n4}
LshapedFfCenter	$pQ13$	norm	logistic	logistic	logistic
	$pQ14$	norm	logistic	logistic	norm
	$pQ15$	logistic	norm	logistic	norm

Source: Author's production.

For the first natural frequency, ω_n, the percentage between free porosity state and acceptable state, Table 6.6, is bigger than the obtained for the beam case. As for the probability distributions, the three porosity cases cover a similar region. It is possible to interpret that besides a frequency decay, there still would not be possible to obtain a significant conclusion about porosity presence only based on natural frequency measures. An interesting behavior, different from the ones obtained for the beam, was the natural frequency increase for mode three, ω_{n3}. This can be interpreted as the porosity distribution in the central area generating a stiffness increase effect for the structure for third mode.

If a hypothesis was set as a variation pattern between the four natural frequencies following Table 6.6, a porosity identification could potentially be performed. Spatial distribution is more complex in the L-shape because the porosity combinations have a

Table 6.6 – L-shape natural frequency mean [Hz].

	ω_{n1}	ω_{n2}	ω_{n3}	ω_{n4}	ηf
0	16926.912	36118.408	39054.769	42312.398	0.00E+00
$pQ13$	16798.734	36021.931	39296.023	42238.355	1.94E-05
$pQ14$	16760.761	36000.464	39287.681	42195.897	2.02E-04
$pQ15$	16748.834	36001.685	39286.605	42170.391	2.54E-04

Source: Author's production.

Figure 6.13 – Natural frequency behavior with increase porosity quantity - LshapedFf-Center.

(a) Natural frequency ω_{n1} x Porosity quantity

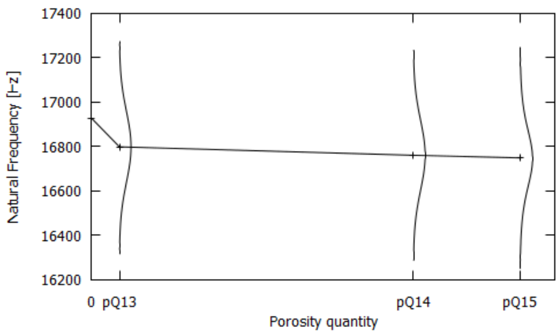

(b) Natural frequency ω_{n2} x Porosity quantity

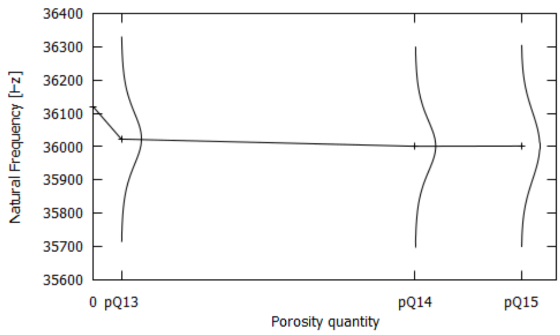

(c) Natural frequency ω_{n3} x Porosity quantity

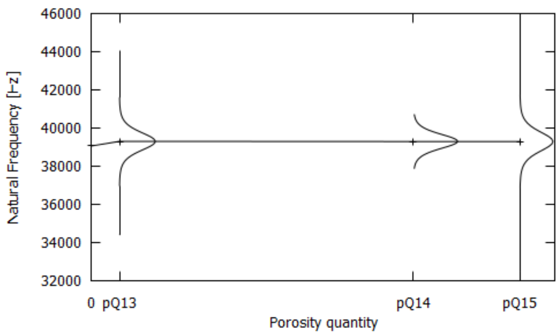

(d) Natural frequency ω_{n4} x Porosity quantity

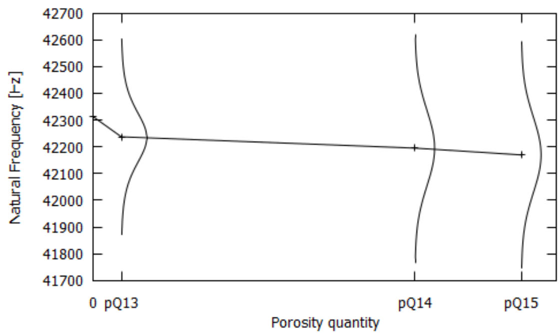

Source: Author's production.

Table 6.7 – L-shaped natural frequency percentage reduction - free porosity / acceptable porosity state.

	ω_{n1}	ω_{n2}	ω_{n3}	ω_{n4}
LshapedFfCenter	0.98%	0.33%	-0.60%	0.28%

Source: Author's production.

more significant impact on the natural frequencies in relation to the beam, resulting in more variability to the data. More realizations can improve the variability, but were not possible in this work due to long simulation times and time constraints.

Figure 6.14 – Free-free L-shape vibration modes.

(a) First vibration mode.

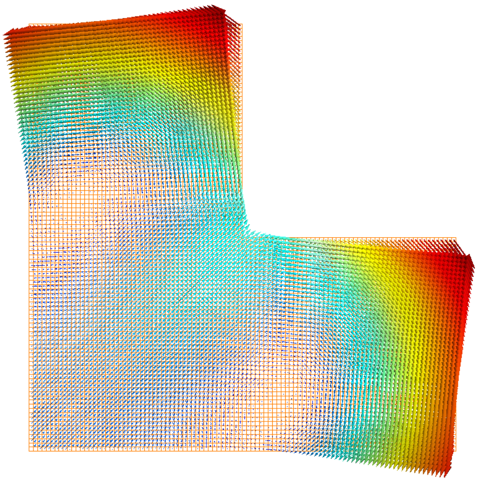

(b) Second vibration mode.

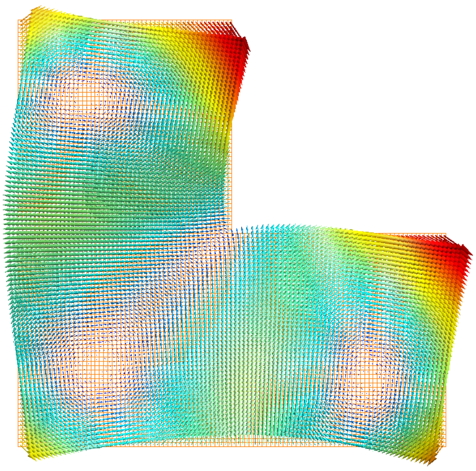

(c) Third vibration mode.

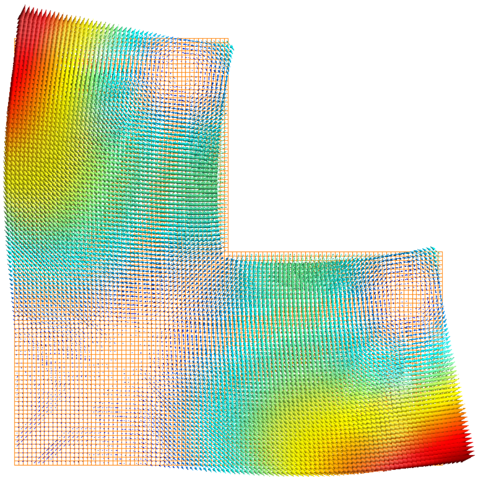

(d) Fourth vibration mode.

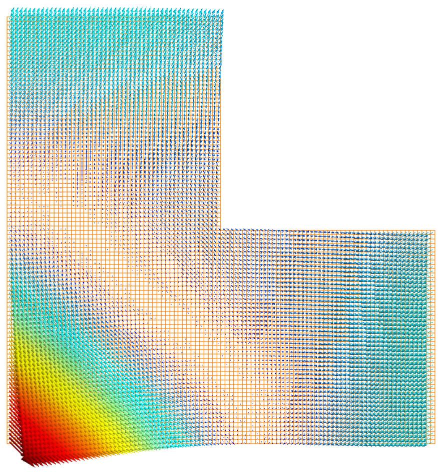

Source: Author's production.

Chapter 7

Conclusions

A numerical formulation based on probability distributions and finite element method capable of representing different porosity levels and spatial distributions is proposed.

Acceptable porosity states were determined based on reference radiography image and reproduced with the numerical formulation.

Applying the Monte Carlo Simulation method, different porosity levels and spatial distributions were generated to calculate the respective natural frequencies with statistical relevance. With a statistical background, it was possible to represent the natural frequencies through probability distributions.

Porosities dispersed through all the structures, independent of the fixation method, produced a decrease of the natural frequency with the increase of porosity quantity for the first four vibrations modes. The same is also found when porosities are restricted in the extremities along X-axis of a beam.

No significant changes in natural frequencies are observed for porosities constraint to the neutral plane region, allowing no porosity identification in these regions using only natural frequency from bending modes. An evaluation considering natural frequency from axial modes could provide more information for this case.

A pattern with significant reduction on the first natural frequency than in the other frequencies can represent porosity concentration in the fixture region for a clamped beam.

The L-shaped structure allows for more complex porosity spatial distribution, and despite an observed natural frequency reduction, no identification pattern is possible because of the elevated variability of the responses.

In conclusion, porosity distributions can be mapped and patterns can be established with vibration-based models. Casting quality control, for example, could use this approach to identify acceptable porosity levels in casting components.

7.1 Future work

Further analysis considering frequency response functions could lead to a more significant conclusion regarding porosity identification since others parameters are extracted.

Numerical models considering equivalent homogeneous material as a way to represent the porosity level to improve simulation time.

Study alternative methods for Monte Carlo Simulation Method for collect different porosity levels and spatial distributions with the target of reducing the computational cost.

Bibliography

ABIFA. *Índices Setoriais*. 2020. Disponível em: <https://www.abifa.org.br/indices-setoriais/>.

ALVA, A.; DESAI, V. Damping behaviour of cast and sintered aluminium. 01 2006.

ASTM E505-15. *E505-15 Standard Reference Radiographs for Inspection of Aluminum and Magnesium Die Castings*. [S.l.], 2000. Disponível em: <https://doi.org/10.1520/E0505-15>.

AVALLE, M. et al. Casting defects and fatigue strength of a die cast aluminium alloy: a comparison between standard specimens and production components. *International Journal of Fatigue*, v. 24, n. 1, p. 1–9, 2002.

Chapter 17 - filtration and the running and gating of iron castings. In: BROWN, J. R. (Ed.). *Foseco Ferrous Foundryman's Handbook (Eleventh Edition)*. Eleventh edition. Oxford: Butterworth-Heinemann, 2000. p. 245–271. ISBN 978-0-7506-4284-2. Disponível em: <https://www.sciencedirect.com/science/article/pii/B9780750642842500181>.

Chapter 19 - feeding of castings. In: BROWN, J. R. (Ed.). *Foseco Ferrous Foundryman's Handbook (Eleventh Edition)*. Eleventh edition. Oxford: Butterworth-Heinemann, 2000. p. 296–II. ISBN 978-0-7506-4284-2. Disponível em: <https://www.sciencedirect.com/science/article/pii/B978075064284250020X>.

BUFFIèRE, J.-Y. et al. Experimental study of porosity and its relation to fatigue mechanisms of model al–si7–mg0.3 cast al alloys. *Materials Science and Engineering: A*, v. 316, n. 1, p. 115–126, 2001. ISSN 0921-5093. Disponível em: <https://www.sciencedirect.com/science/article/pii/S0921509301012254>.

CARLSON, K. D. et al. Modeling of porosity formation and feeding flow in steel casting. n. 4.4, 2002.

DAMIR, A.; ELKHATIB, A.; NASSEF, G. Prediction of fatigue life using modal analysis for grey and ductile cast iron. *International Journal of Fatigue*, v. 29, p. 499–507, 03 2007.

DOEBLING, S.; FARRAR, C.; PRIME, M. A summary review of vibration-based damage identification methods. *The Shock and Vibration Digest*, v. 30, p. 91–105, 03 1998.

EWINS, D. *Modal Testing: Theory, Practice and Application*. Wiley, 2000. (Engineering dynamics series]). ISBN 9780863802188. Disponível em: <https://books.google.com.br/books?id=Z4QoAQAAMAAJ>.

GAO, Y. et al. The effect of porosity on the fatigue life of cast aluminium-silicon alloys. *Fatigue & Fracture of Engineering Materials & Structures*, Wiley Online Library, v. 27, n. 7, p. 559–570, 2004.

HINTON, E.; ROCK, T.; ZIENKIEWICZ, O. A note on mass lumping and related processes in the finite element method. *Earthquake Engineering & Structural Dynamics*, Wiley Online Library, v. 4, n. 3, p. 245–249, 1976.

HUGHES, T. *The Finite Element Method: Linear Static and Dynamic Finite Element Analysis*. Dover Publications, 2000. (Dover Civil and Mechanical Engineering). ISBN 9780486411811. Disponível em: <https://books.google.com.br/books?id=yarmSc7ULRsC>.

JEARY, A. Damping in structures. *Journal of Wind Engineering and Industrial Aerodynamics*, v. 72, p. 345–355, 1997. ISSN 0167-6105. Selected papers from the Ninth International Symposium on Wind Engineering. Disponível em: <https://www.sciencedirect.com/science/article/pii/S0167610597002638>.

KESSLER, S. S. et al. Damage detection in composite materials using frequency response methods. *Composites Part B: Engineering*, Elsevier, v. 33, n. 1, p. 87–95, 2002.

KHALAJZADEH, V.; BECKERMANN, C. Simulation of shrinkage porosity formation during alloy solidification. *Metallurgical and Materials Transactions A*, v. 51, 03 2020.

KHALAJZADEH, V.; GOETTSCH, D.; BECKERMANN, C. Real-time x-ray radiography and computational modeling of shrinkage porosity formation in aluminum alloy castings. *Metallurgical and Materials Transactions A*, v. 50, p. 1–15, 11 2018.

KUBO, K.; PEHLKE, R. D. Mathematical modeling of porosity formation in solidification. *Metallurgical Transactions B*, Springer, v. 16, n. 2, p. 359–366, 1985.

LEAL, T. S. *Avaliação numérica-experimental do processo de solidificação de alumínio com predição de porosidade*. Tese (dissertation) — Universidade do Estado de Santa Catarina, 2019. Disponível em: <https://sistemabu.udesc.br/pergamumweb/vinculos/000067/00006746.pdf>.

LEE, P.; CHIRAZI, A.; SEE, D. Modeling microporosity in aluminum–silicon alloys: a review. *Journal of Light Metals*, v. 1, n. 1, p. 15–30, 2001. ISSN 1471-5317. Disponível em: <https://www.sciencedirect.com/science/article/pii/S1471531700000031>.

LEHOUCQ, R. B.; SORENSEN, D. C.; YANG, C. *ARPACK Users' Guide*. Society for Industrial and Applied Mathematics, 1998. Disponível em: <https://epubs.siam.org/doi/abs/10.1137/1.9780898719628>.

MONTERO, D. S. *Topology optimization of continuum structures subjected to harmonic loads with local stress constraints*. Tese (dissertation) — Universidade do Estado de Santa Catarina, 2019. Disponível em: <https://sistemabu.udesc.br/pergamumweb/vinculos/000067/00006744.pdf>.

MONTGOMERY, D.; RUNGER, G. *Applied Statistics and Probability for Engineers*. John Wiley & Sons, 2010. ISBN 9780470053041. Disponível em: <https://books.google.com.br/books?id=_f4KrEcNAfEC>.

NADCA. *NADCA product specification standards for die casting: aluminum, aluminum-MMC, copper, magnesium, zinc and ZA alloys*. [S.l.], 2015. Disponível em: <https://doi.org/10.1520/E0505-15>.

NEWMAN, M. E. J.; BARKEMA, G. T. *Monte Carlo methods in statistical physics*. Oxford: Clarendon Press, 1999.

OSMOND, P. et al. Effect of porosity on the fatigue strength of cast aluminium alloys: from the specimen to the structure. *Procedia Engineering*, v. 213, p. 630–643, 01 2018.

OWOLABI, G.; SWAMIDAS, A.; SESHADRI, R. Crack detection in beams using changes in frequencies and amplitudes of frequency response functions. *Journal of sound and vibration*, Elsevier, v. 265, n. 1, p. 1–22, 2003.

PEDERSEN, N. Maximization of eigenvalues using topology optimization. *Structural and Multidisciplinary Optimization*, v. 20, p. 2–11, 01 2000.

PIWONKA, T.; FLEMINGS, M. Pore formation in solidification. *Aime Met Soc Trans*, v. 236, n. 8, p. 1157–1165, 1966.

RAO, S. S.; FAH, Y. F. *Mechanical vibrations; 5th ed. in SI units*. Singapore: Prentice Hall, 2011. Disponível em: <https://cds.cern.ch/record/1398617>.

SABAU, A.; VISWANATHAN, S. Porosity prediction in aluminuma356 alloy castings. *Oak Ridge, Tennessee*, Citeseer, 2008.

SATA, A. V. *Shrinkage Porosity Prediction Using Casting Simulation*. Tese (dissertation) — Indian Institute of Technology Bombay, 2010. Disponível em: <http://efoundry.iitb.ac.in/TechnicalPapers/dissertations/AMIT\%20SATA\%202010.pdf>.

SAVELLI, S.; BUFFIERE, J.-y.; FOUGèRES, R. Pore characterization in a model cast aluminum alloy and its quantitative relation to fatigue life studied by synchrotron x-ray microtomography. *Materials Science Forum*, v. 331-337, p. 197–202, 05 2000.

TANDON, K.; BEGIN, J. A study of variation in the natural frequency of steel castings containing porosity and inclusions. *Applied Acoustics*, v. 29, n. 3, p. 219–227, 1990. ISSN 0003-682X. Disponível em: <https://www.sciencedirect.com/science/article/pii/0003682X9090020U>.

THODE, H. C. Normality tests. In: ______. *International Encyclopedia of Statistical Science*. Berlin, Heidelberg: Springer Berlin Heidelberg, 2011. p. 999–1000. ISBN 978-3-642-04898-2. Disponível em: <https://doi.org/10.1007/978-3-642-04898-2_423>.

WANG, G.; APELIAN, D.; LADOS, D. Fatigue behavior of a356-t6 aluminum cast alloys. part i. effect of casting defects. *Journal of Light Metals*, v. 1, p. 73–84, 02 2001.

Whittenberger, E. J.; Rhines, F. N. Origin of Porosity in Castings of Magnesium-Aluminum and Other Alloys. *JOM - Journal of the Minerals, Metals and Materials Society*, v. 4, n. 4, p. 409–420, abr. 1952.

YANG, X. et al. A kriging model based finite element model updating method for damage detection. *Applied Sciences*, v. 7, p. 1039, 10 2017.

YI, J. et al. Scatter in fatigue life due to effects of porosity in cast a356-t6 aluminum-silicon alloys. *Metallurgical and Materials Transactions A*, v. 34, p. 1879–1890, 09 2003.

Appendix A

Convergence graphs

Figure A.1 – Convergence of the mean and std with increase iterations for the beamFfAll

(a) Frequency Mean × Iterations - ω_{n1}

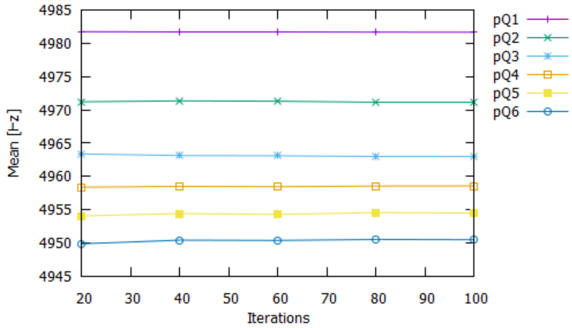

(b) Frequency Std × Iterations - ω_{n1}

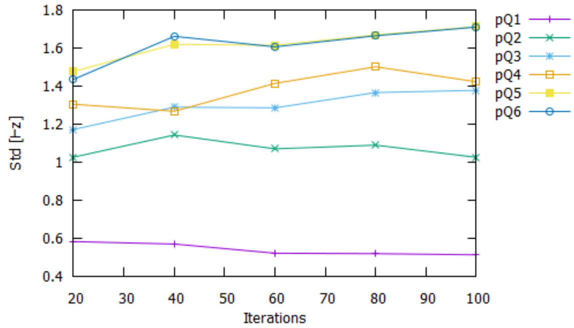

(c) Frequency Mean × Iterations - ω_{n2}

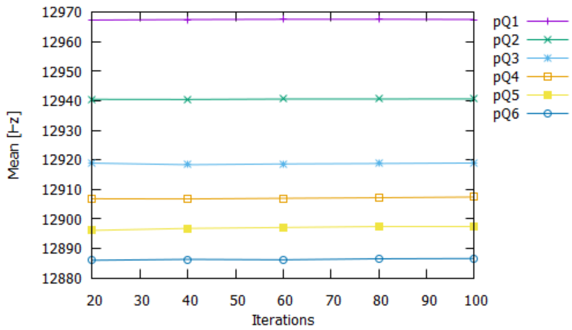

(d) Frequency Std × Iterations- ω_{n2}

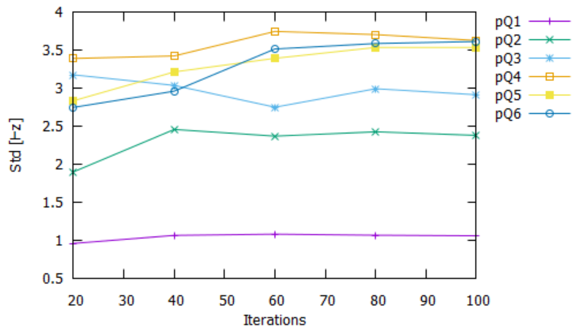

(e) Frequency Mean × Iterations - ω_{n3}

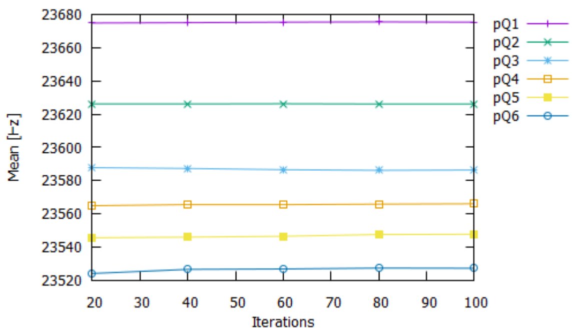

(f) Frequency Std × Iterations- ω_{n3}

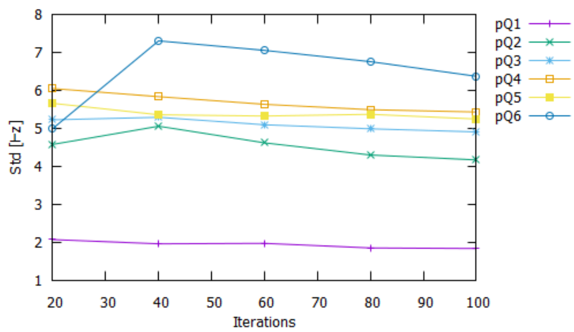

(g) Frequency Mean × Iterations - ω_{n4}

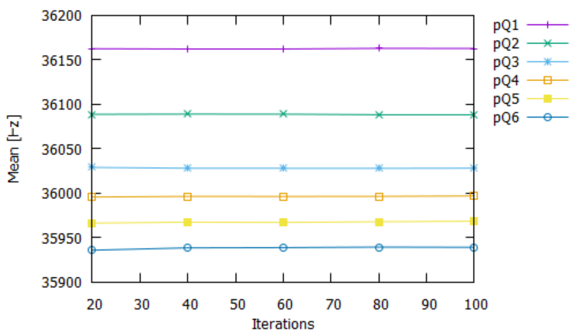

(h) Frequency Std × Iterations- ω_{n4}

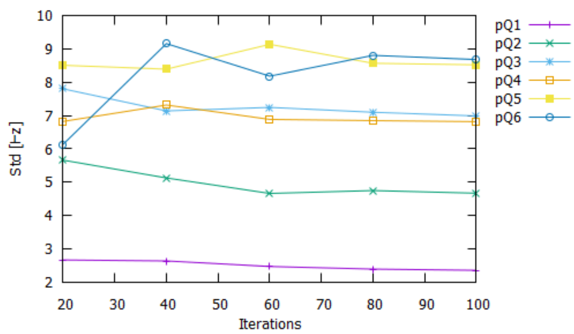

Source: Author's production

Figure A.2 – Convergence of the mean and std with increase iterations for the beamFfExtX

(a) Frequency Mean $\times$ Iterations - ω_{n1}

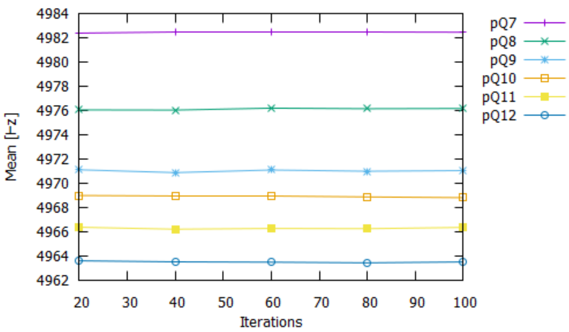

(b) Frequency Std $\times$ Iterations - ω_{n1}

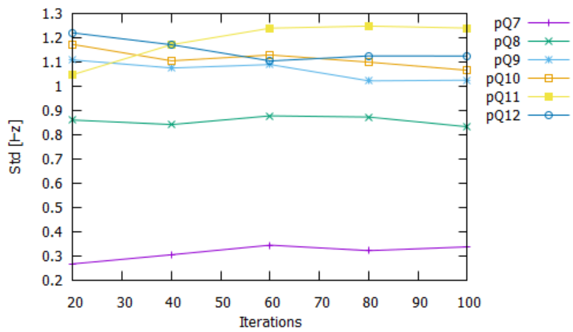

(c) Frequency Mean $\times$ Iterations - ω_{n2}

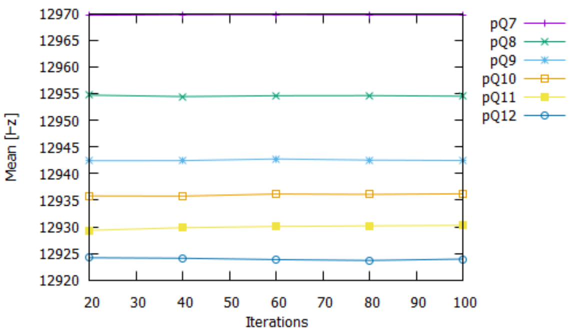

(d) Frequency Std $\times$ Iterations- ω_{n2}

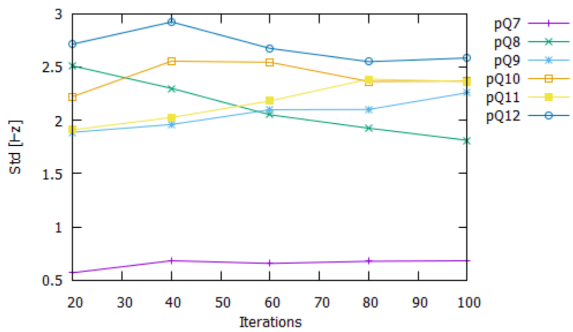

(e) Frequency Mean $\times$ Iterations - ω_{n3}

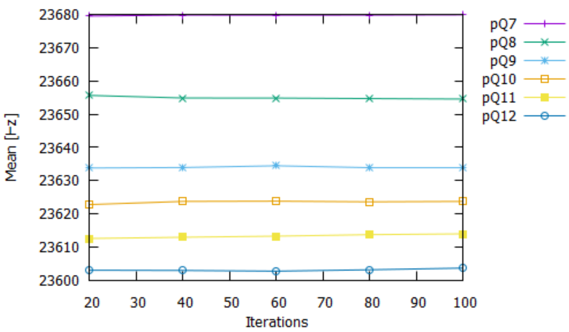

(f) Frequency Std $\times$ Iterations- ω_{n3}

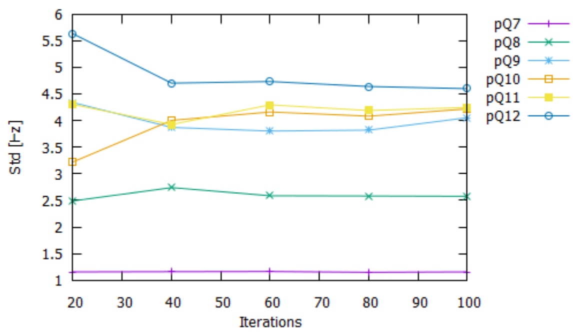

(g) Frequency Mean $\times$ Iterations - ω_{n4}

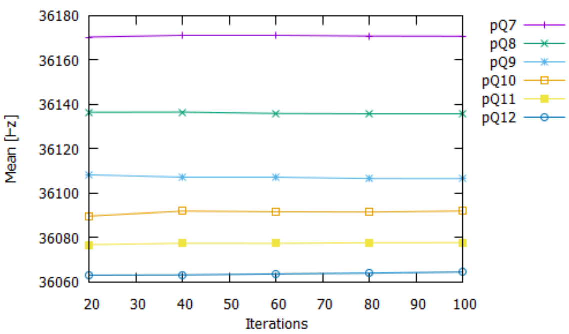

(h) Frequency Std $\times$ Iterations- ω_{n4}

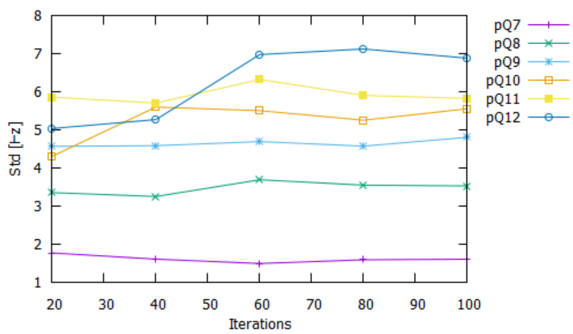

Source: Author's production

Figure A.3 – Convergence of the mean and std with increase iterations for the beamFfLmX

(a) Frequency Mean $\times$ Iterations - ω_{n1}

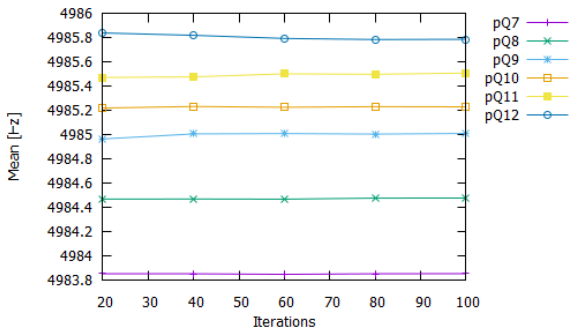

(b) Frequency Std $\times$ Iterations - ω_{n1}

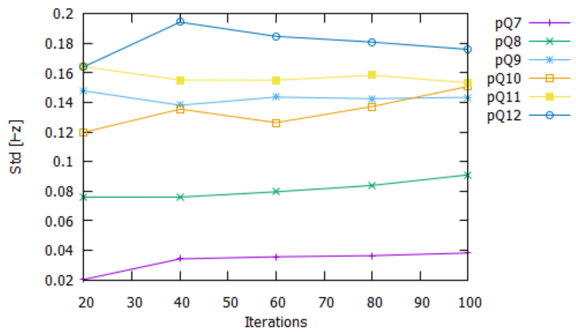

(c) Frequency Mean $\times$ Iterations - ω_{n2}

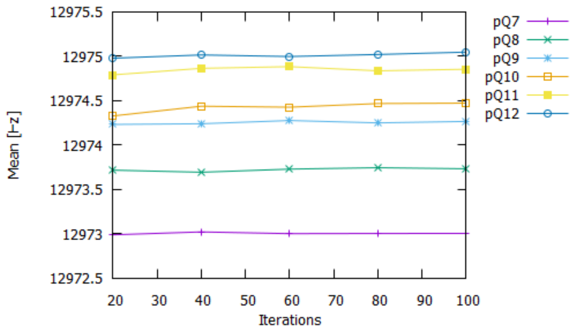

(d) Frequency Std $\times$ Iterations- ω_{n2}

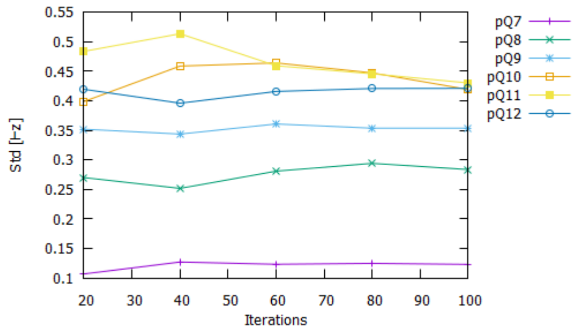

(e) Frequency Mean $\times$ Iterations - ω_{n3}

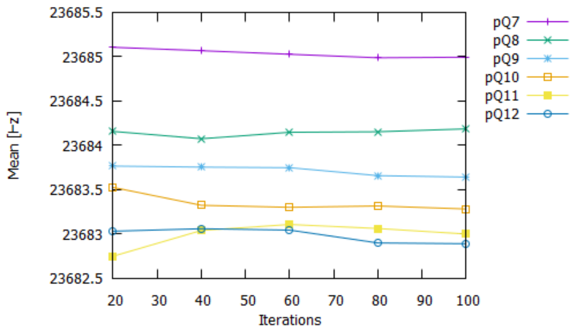

(f) Frequency Std $\times$ Iterations- ω_{n3}

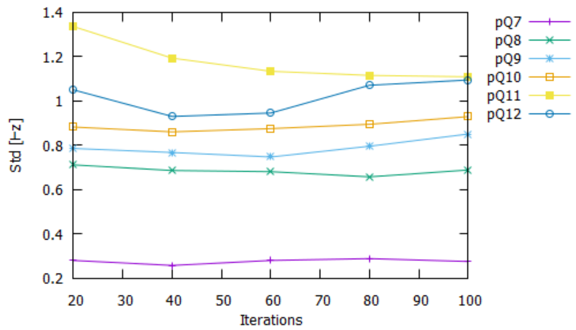

(g) Frequency Mean $\times$ Iterations - ω_{n4}

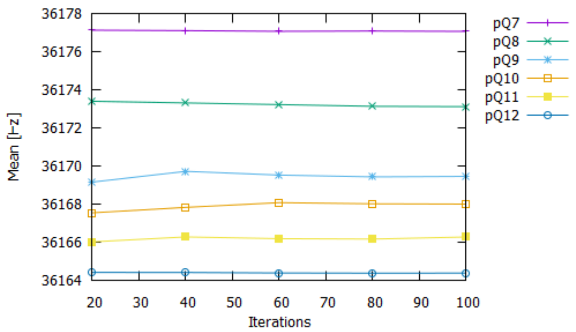

(h) Frequency Std $\times$ Iterations- ω_{n4}

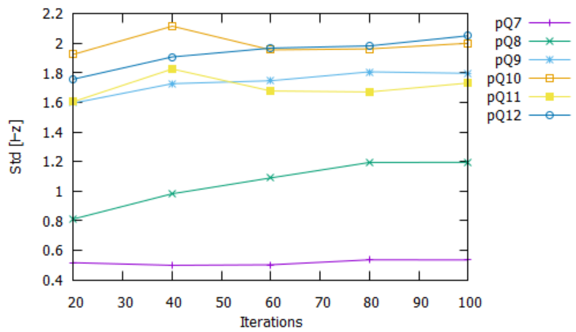

Source: Author's production

Figure A.4 – Convergence of the mean and std with increase iterations for the beamFixfAll

(a) Frequency Mean × Iterations - ω_{n1}

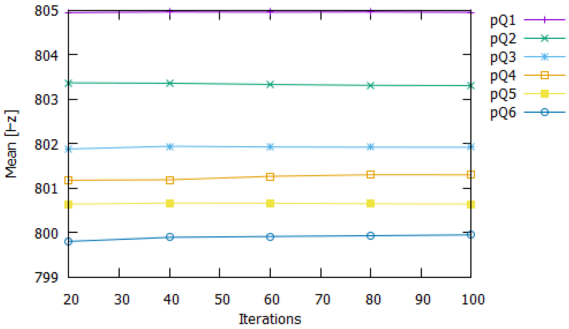

(b) Frequency Std × Iterations - ω_{n1}

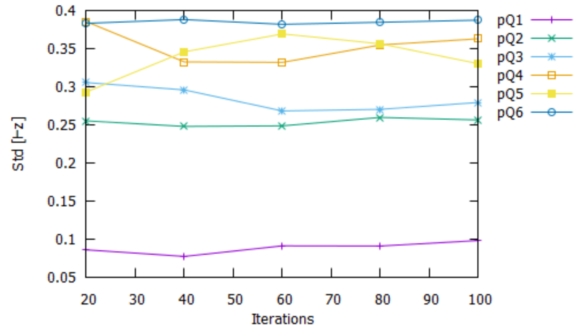

(c) Frequency Mean × Iterations - ω_{n2}

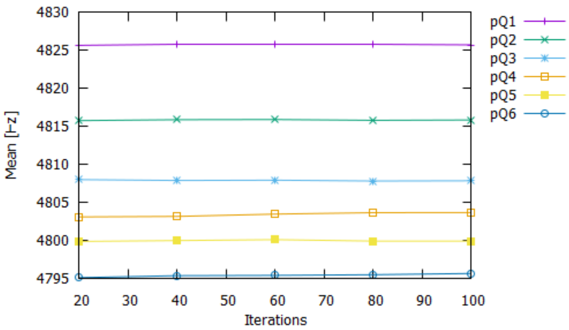

(d) Frequency Std × Iterations- ω_{n2}

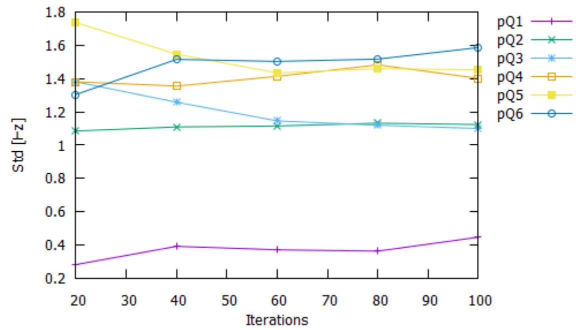

(e) Frequency Mean × Iterations - ω_{n3}

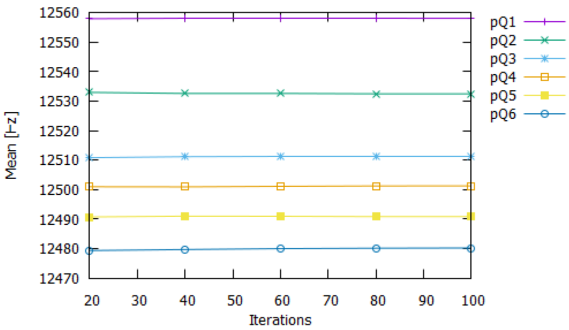

(f) Frequency Std × Iterations- ω_{n3}

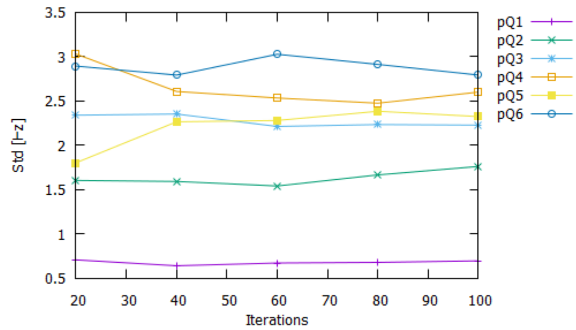

(g) Frequency Mean × Iterations - ω_{n4}

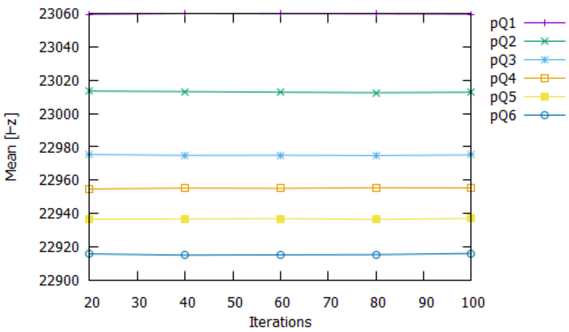

(h) Frequency Std × Iterations- ω_{n4}

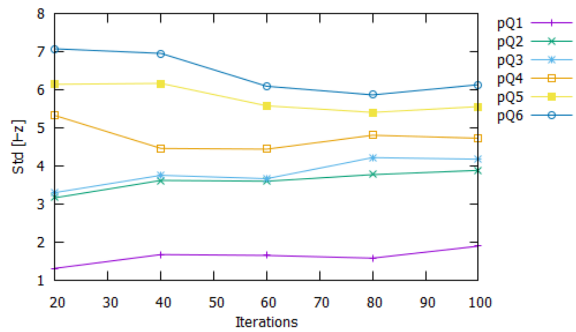

Source: Author's production

Figure A.5 – Convergence of the mean and std with increase iterations for the beamFixfAll

(a) Frequency Mean $\times$ Iterations - ω_{n1}

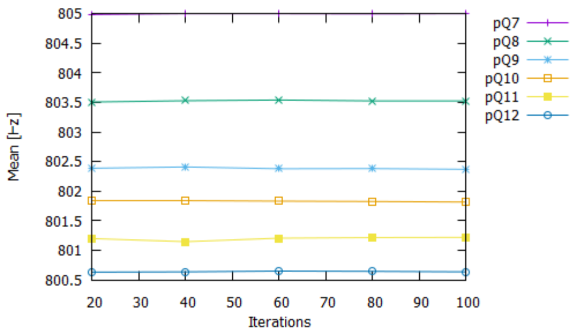

(b) Frequency Std $\times$ Iterations - ω_{n1}

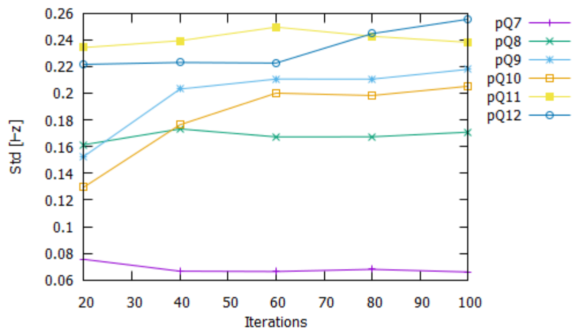

(c) Frequency Mean $\times$ Iterations - ω_{n2}

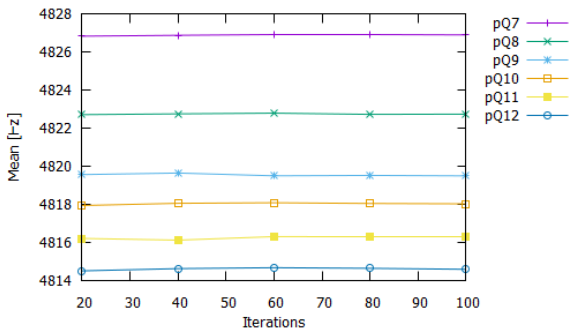

(d) Frequency Std $\times$ Iterations- ω_{n2}

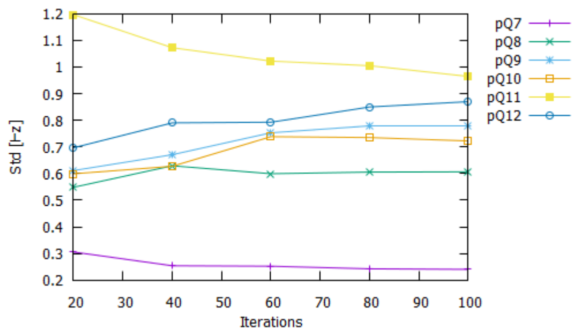

(e) Frequency Mean $\times$ Iterations - ω_{n3}

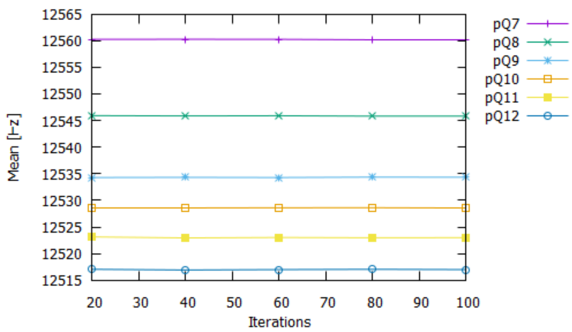

(f) Frequency Std $\times$ Iterations- ω_{n3}

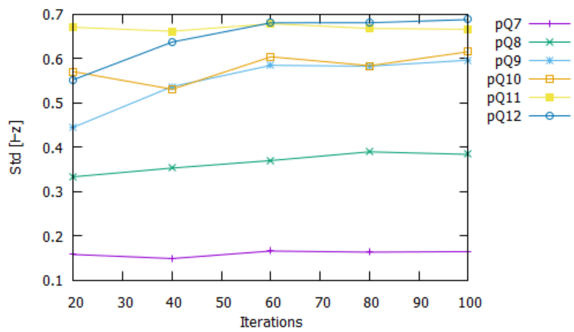

(g) Frequency Mean $\times$ Iterations - ω_{n4}

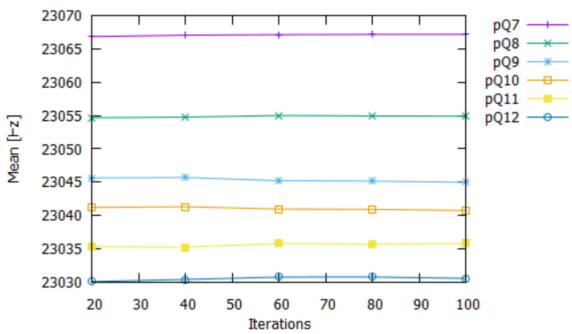

(h) Frequency Std $\times$ Iterations- ω_{n4}

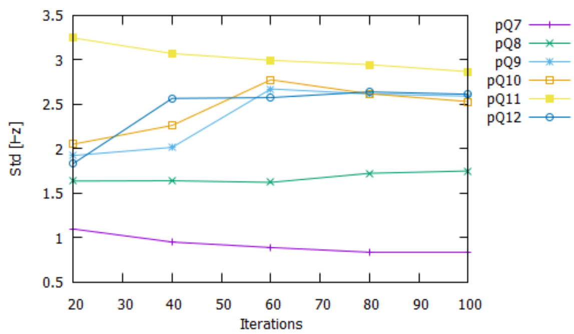

Source: Author's production

Figure A.6 – Convergence of the mean and std with increase iterations for the bootFf-Center

(a) Frequency Mean $\times$ Iterations - ω_{n1}

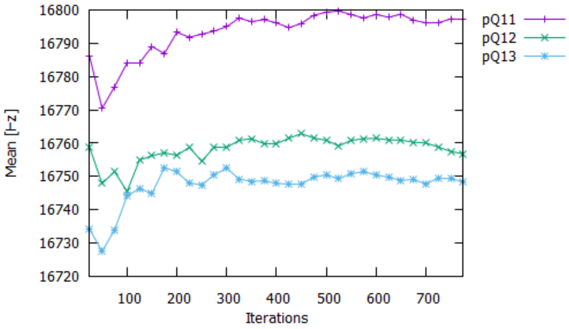

(b) Frequency Std $\times$ Iterations - ω_{n1}

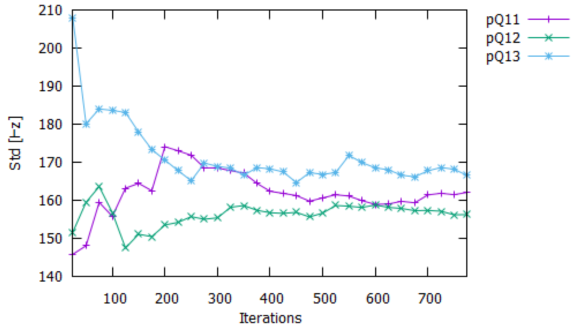

(c) Frequency Mean $\times$ Iterations - ω_{n2}

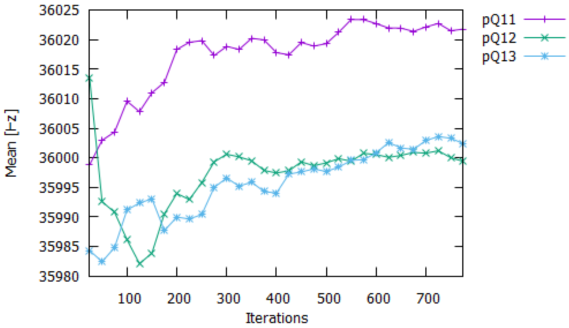

(d) Frequency Std $\times$ Iterations- ω_{n2}

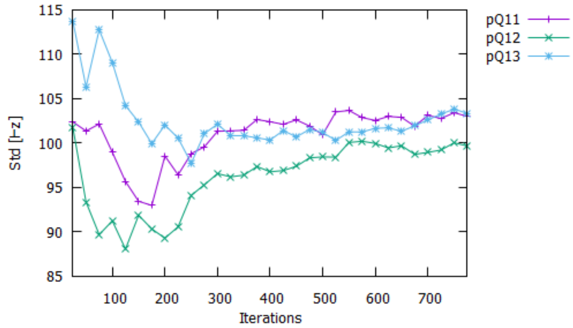

(e) Frequency Mean $\times$ Iterations - ω_{n3}

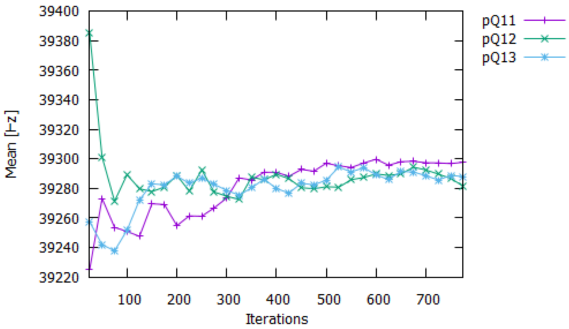

(f) Frequency Std $\times$ Iterations- ω_{n3}

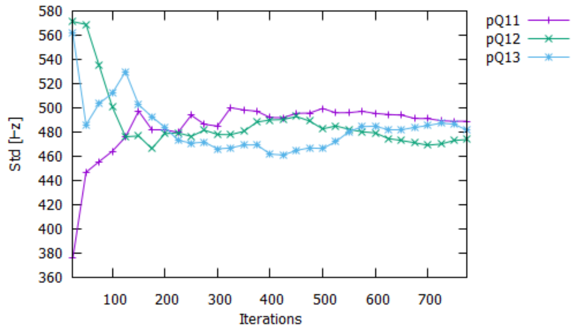

(g) Frequency Mean $\times$ Iterations - ω_{n4}

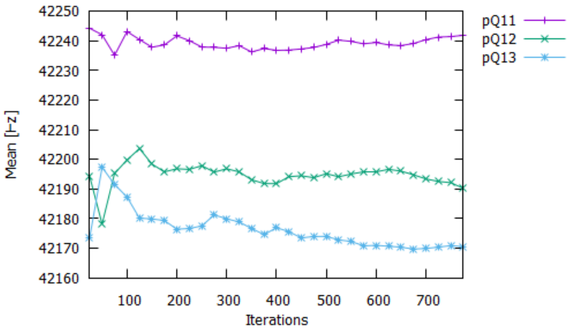

(h) Frequency Std $\times$ Iterations- ω_{n4}

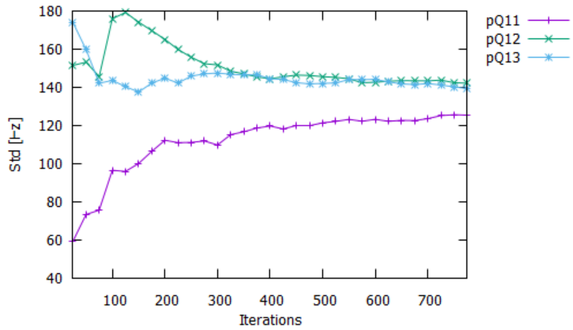

Source: Author's production